Journal of Membrane Science 693 (2024) 122337

Contents lists available at ScienceDirect

Journal of Membrane Science

journal homepage: www.elsevier.com/locate/memsci

High-performance hydrogen separation using cellulose-based carbon molecular sieve membranes

Tiago Araújo [a,b], Gabriel Bernardo [a,b], Adélio Mendes [a,b,*]

[a] LEPABE – Laboratory for Process Engineering, Environment, Biotechnology and Energy, Faculty of Engineering, University of Porto, Rua Dr. Roberto Frias, 4200-465, Porto, Portugal
[b] AliCE – Associate Laboratory in Chemical Engineering, Faculty of Engineering, University of Porto, Rua Dr. Roberto Frias, 4200-465, Porto, Portugal

ARTICLE INFO

Keywords:
Carbon membrane
Hydrogen recovery
Cellulose
Process design
Economic analysis

ABSTRACT

Cellulose-based carbon molecular sieve membranes were designed for hydrogen deblending from natural gas and hydrogen recovery from other relevant industrial sources. The crystallinity of the cellulose precursor was increased by adding propylene glycol, which originated a carbon membrane with a permeability to the hydrogen of 544 barrer and an H_2/CH_4 permselectivity of *ca.* 3500 (Robeson index = 100). A careful optimization of the carbonization conditions of the cellulose precursor boosted the carbon membrane permeability to hydrogen to 1144 barrer and the H_2/CH_4 permselectivity to 1080 (Robeson index = 62). The membrane with the highest permeability to hydrogen presented the highest micropore volume of 0.443 $cm^3 \cdot g^{-1}$ and a micropore surface area of 1326 $m^2 \cdot g^{-1}$.

A detailed techno-economic analysis of the hydrogen recovery from the natural gas was performed. It was concluded that a single-stage carbon membrane module can recover hydrogen with a concentration of 99.8 % and a specific cost of 0.26 $€ \cdot kgH_2^{-1}$ for a hydrogen recovery of 68 %. A two-stage membrane process was simulated to deliver a purity >99.997 % and a recovery of 96 %, with a specific cost of 1.8 $€ \cdot kgH_2^{-1}$. The carbon membranes prepared in this work are highly competitive with other separation processes for the recovery and purification of hydrogen from different industrial processes essential for the decarbonization.

1. Introduction

Energy from renewable sources and carbon capture utilization and storage (CCUS) strategies have been considered by several countries to reduce CO_2 emissions into the atmosphere [1]. An energy carrier, such as hydrogen (H_2), has been pointed out as an alternative energy vector due to its high energy-to-mass ratio [2]; namely, H_2 was pointed out for replacing coal and natural gas in fossil fuel-intensive industries. According to the International Energy Agency (IEA), H_2 consumption should increase in the 2070s to about seven times its value in 2020 [3]. H_2 can be used as a vehicle fuel, in fuel cells for electricity production, and as a feedstock to produce synthetic fuels, chemicals, and fertilizer [4].

Hydrogen does not exist in the Earth in its molecular state, so it must be produced from renewable sources. There are presently four types of processes for producing hydrogen from renewable sources, though at different stages of development: chemically, thermochemically, biologically, and electrochemically [5]. Almost 96 % of the hydrogen is nowadays produced from the reforming of fossil fuels (coal and natural gas) [6]. Some studies show that the cheapest processes to produce hydrogen are by steam methane reforming (SMR), with a production cost of *ca.* 5.6 $€ \cdot kgH_2^{-1}$, and by methane splitting (MS, also known as methane decomposition or methane cracking), with a production cost of 5.0 $€ \cdot kgH_2^{-1}$ [5]. Electrochemical processes including the water electrolysis, such as alkaline, PEM-electrolysis, AEM-electrolysis, and SOE require a great amount of energy for splitting the water molecule [5]. Therefore, if there is no cheap green electricity, water electrolysis may become economically less attractive.

Besides the production challenges, the so-called hydrogen economy must overcome the transport and storage of a fuel, which has an extremely low volumetric density. Even at 700 bar, the hydrogen energy density is just 1.3 $kWh \cdot L^{-1}$, compared with the energy of gasoline, which is *ca.* 10 $kWh \cdot L^{-1}$ [4]. Transporting and distributing hydrogen seems to be, however, a greater challenge [7]. Hydrogen can be transported in

* Corresponding author. LEPABE – Laboratory for Process Engineering, Environment, Biotechnology and Energy, Faculty of Engineering, University of Porto, Rua Dr. Roberto Frias, 4200-465 Porto, Portugal.
E-mail address: mendes@fe.up.pt (A. Mendes).

https://doi.org/10.1016/j.memsci.2023.122337
Received 2 November 2023; Received in revised form 6 December 2023; Accepted 9 December 2023
Available online 14 December 2023

tankers or ships, liquefied; however, the liquefaction process consumes the equivalent of 36 % of the internal energy of hydrogen, and the energy density is just 2.3 $kWh{\cdot}L^{-1}$ [8]. The cheapest way to transport hydrogen is by pipeline [9]; conversely, it can be transformed into methanol or ammonia for easier and cheaper storage and transport [10]. However, pipeline transport is still challenging even though many European countries (namely Portugal [11,12]) are already building infrastructures or using the existing infrastructure for natural gas to transport hydrogen [13]. Compared with constructing a new pipeline, using existing natural gas pipelines for transporting hydrogen can decrease transportation costs by more than 60 % [13], but partially retrieving the injected hydrogen (normally up to 10 %) requires an efficient and low-cost deblending technology [14].

Conventional cryogenic distillation and pressure swing adsorption (PSA) separation technologies, due to their high energy consumption, have yet to demonstrate to be efficient in recovering and purifying hydrogen from natural gas streams [15]. The H_2 recovery cost using a PSA unit was estimated to be 8 $€{\cdot}kgH_2^{-1}$ [16]. Membrane separators, due to their procedural simplicity, low energy demand, scalability, and high hydrogen separation efficiency, are excellent candidates for the on-site H_2 recovery from the natural gas network [16,17]. Moreover, the membrane feed does not need to be compressed since the pressure in the pipeline is already quite high, in the range of 8–60 bar [16,18] (Fig. 1).

High-purity H_2 is easy to deblending from natural gas using palladium/silver membranes due to their high permeance and selectivity [19]. However, the high price of palladium and its scarcity, besides the potential surface poisoning by natural gas contaminants, make this technology unattractive [18]. On the other hand, polymeric membranes are low-cost and easy to produce but they display low selectivities [4,18]. Carbon molecular sieve membranes (CMSM) are nowadays the most promising membrane technology for hydrogen separations [18]. Their rigid structure with micropores and ultramicropores, resulting from the controlled decomposition of polymeric precursors at high temperatures, favors the high permeabilities and selectivities necessary for the selective separation of hydrogen from bulkier molecules such as carbon dioxide (CO_2), nitrogen (N_2), methane (CH_4) or hydrocarbons [20,21]. CMSM are promising for separations at high temperatures, high pressure, and harsh environments due to their high stability [22]. Compared to other membrane technologies, CMSMs have the best H_2/CH_4 separation performance with permeabilities and selectivities well above the Robeson "upper bound" [4]. A variety of polymeric precursors can be used to produce CMSM, such as polyimides [23,24], phenolic resins [25–27], or cellulose [28,29]. They can be used supported or unsupported. The great H_2 separation potential for supported polyimide-based CMSM with a selective layer of 200 nm was reported by Ngamou et al. with an permeance to H_2 of 1.1×10^{-6} $mol{\cdot}m^{-2}{\cdot}s^{-1}{\cdot}Pa^{-1}$ (657 barrer) and an H_2/CH_4 selectivity of 228 at 220 °C (Robeson Index of 7.9) [30]. Losa Tanco et al., prepared supported CMSM with a phenolic resin precursor and obtained H_2 permeances of 50.4×10^{-9} $mol{\cdot}m^{-2}{\cdot}s^{-1}{\cdot}Pa^{-1}$ (1620 barrer) at 30 °C with an H_2/CH_4 selectivity of 435 (Robeson Index of 34), which dropped to 37 at 80 °C [26]. These authors found that this membrane was an excellent candidate for deblending hydrogen from natural gas; when feeding the membrane at 30 °C with a 10 % hydrogen mixture in methane, the authors obtained a permeate stream containing 99.4 % of hydrogen for a pressure ratio of 750; the membrane has a permeability to hydrogen of 750 barrer and a selectivity to H_2/CH_4 selectivity of 1540 (*ca.* 3.5 times higher than the single gas selectivity – Robeson Index of 60) [26]. In other work, those same CMSMs were compared with Ag–Pd membranes, and the authors concluded that CMSMs are preferable for high-purity H_2 production when operating at higher pressures and lower temperatures (30 °C) [17]. In that work, the authors found that the support of the CMSMs have a major contribution to the membrane cost, which then impacts the cost of H_2 purification [17]. A specific cost of 4.44 $€{\cdot}kgH_2^{-1}$ was obtained to purify 25 $kgH_2{\cdot}day^{-1}$ with a purity of 99 % from a feed contenting 10 % of hydrogen in natural gas [16]. Therefore, unsupported or asymmetric thin membranes produced from low-cost and abundant polymeric precursors should be investigated to reduce the production costs of the CMSM; thinner membranes display higher permeances and then originate membrane modules with higher productivity. CMSMs prepared by Rodrigues et al. [28] from a cellulose precursor showed great separation performance indicators, high stability and tunability, reproducibility, and low production costs; they demonstrated a stable separation performance, even at relative humidities >80 %, due to their hydrophilicity character, which allows the water vapor to permeate very fast [28]. These CMSMs show H_2/CH_4 selectivities >200 000 at 25 °C with a permeability to hydrogen of 206 barrer (Robeson Index of 2500) [31]; though displaying a very high Robeson Index, these membranes should display as well a high permeability to hydrogen to become industrially attractive. Asymmetric CMSM hollow fibers prepared from microcrystalline cellulose with an appropriate drying protocol to prevent pore collapse were reported for efficient and stable H_2 separations in the presence of water vapor [29]. A permeability to H_2 of 444.6 barrer and an H_2/CH_4 selectivity of 5706 (Robeson Index of 139) was obtained operating at 130 °C [29]. The pore structure and surface chemistry of a cellulose-based CMSM can be easily modified to obtain superior separation performances. The authors reported the addition of urea to the cellulose precursor for increasing the micropore volume of the CMSM; the resulting membranes displayed not only an increased permeability to hydrogen, from 305 to 664 barrer, but also kept the ideal selectivity constant to H_2/CH_4 – ~210, allowing an increase in the Robeson index from 3.6 to 7.6 [32].

The separation performance of the CMSMs can be tuned by changing the free volume and/or the crystalline structure of the polymeric precursor. Furthermore, the surface chemistry of the polymeric precursor can also be tuned for different separations. These changes can be obtained by incorporating additives or porogenic agents [33]; applying pre-treatments before carbonization [34]; or changing the carbonization conditions [35], or applying post-treatments. Guo et al. reported the use of poly(styrene sulfonic acid) as a porogenic agent in Tröger's base (TB)

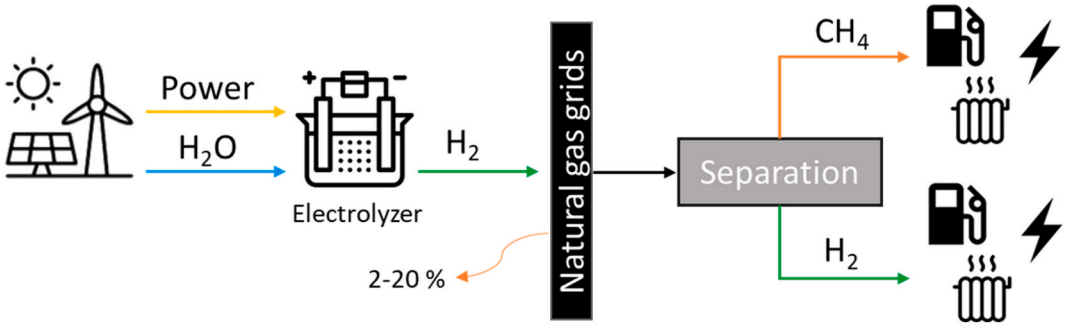

Fig. 1. Scheme of hydrogen production from water electrolysis using power from renewable energy sources and its transportation on existing natural gas grids and post-separation.

polymers, polyimide, and Pebax as an effective approach to produce CMSM with a high permeability to H_2 [33]. A 20 wt% of PSS in a Tröger's base polymer originated, after carbonization at 550 °C, a CMSM displaying a permeability to H_2 of 675 barrer and an H_2/CH_4 selectivity of 552. In contrast, a CMSM prepared from pure TB polymer without PSS, exhibited a permeability to H_2 of 202 barrer with a H_2/CH_4 selectivity of 377. Increasing the carbonization temperature leads to the greater organization of the carbon chains and to pore shrinkage due to their collapse, making CMSMs more selective to small molecules such as H_2 – higher H_2/CH_4 selectivities, though normally at the expense of reducing the membrane permeability [29,35,36]. Besides the temperature history, carbonization conditions can also be adjusted by changing the atmosphere. Ma et al. found that incorporating H_2 into the carbonization purge gas (≤4 %) inhibits the precursor aromatization, resulting in a structure with wider micropores than the CMSM made using an inert atmosphere [37]. Oxygen chemisorption aging can be beneficial to increase the selectivity of the CMSMs; a careful introduction of oxygenated groups into the microporous structure hinders the diffusion of large molecules, making the CMSMs more selective [31].

This work aims at increasing the permeability to hydrogen of CMSMs without compromising their selectivity in mixtures with CO_2, N_2, and CH_4. Therefore, to increase the CMSM selectivity, it was added to the solution of the precursor, an additive with a good affinity to the cellulose matrix - propylene glycol, which contains two hydroxyl groups and one methyl group. Actually, Lei et al. found that using a glycerol softening bath increases the crystallinity of the cellulose precursor and consequently increases the selectivity of the prepared CMSM [34]. However, after this modification, the permeability to H_2 was still low, so H_2 was added to the carbonization gas, which allowed double the permeability of the cellulose-based CMSMs. The selectivity was significantly impaired by adding H_2 to the carbonization atmosphere, so the final carbonization temperature was increased from 550 °C to 630 °C to increase the selectivity. Finally, CMSMs with high permeabilities and H_2/CO_2, H_2/N_2, and H_2/CH_4 selectivity were fabricated, displaying maximum permeability to hydrogen of 1144 barrer. A techno-economic assessment of the developed CMSMs to the hydrogen deblending was performed.

2. Materials and methods

2.1. Materials

Raw pine cellulose (wood pulp), with a degree of polymerization of 450, offered by Innovia Films Ltd. Dimethyl sulfoxide (DMSO) (99.9 %) was acquired from Fisher Scientific. The ionic liquid, 1-ethyl-3-methylimidazolium acetate (Emimac) (≥95 %), and propylene glycol (MPG) (also known as propane-1,2-diol) (≥99.5 %) were purchased from Sigma-Aldrich. Hydrogen (99.999 %), carbon dioxide (99.998 %), nitrogen (99.999 %), and methane (99.995 %) were supplied by Air Liquide.

2.2. Fabrication of the carbon molecular sieve membranes

A solution Emimac:DMSO (30:70 wt%) was used to dissolve the cellulose (9.2 wt%) at 90 °C using magnetic stirring for *ca.* 2 h. The resulting homogeneous mixture was degassed in a vacuum oven for 2 h at 40 °C. The regenerated cellulose-based precursor films were coated on square glass plates (100 cm^2) with a spin coater (POLOS™, SPIN150i) at a spin rate of 1500 rpm with an acceleration of 1000 rpm s^{-1} for 10 s. The coated cellulose films were coagulated in distilled water at room temperature. The films were dried overnight under room conditions. Propylene glycol was added to the cellulose/ionic liquid/DMSO mixture (@ 1 wt%) to modify the crystalline and chemical structure of the regenerated polymeric films. Glycerol and urea were also incorporated at the same concentration (Supplementary Note 1). An illustration of the fabrication method of the precursor films is shown in **Fig. 2**.

The dried precursor films were carbonized in a horizontal furnace (Termolab TH) equipped with a quartz tube (Ø = 8 cm, L = 1.5 m), following the temperature histories sketched in Fig. 3. Nitrogen and a mixture of 5 % of hydrogen balanced with nitrogen were used as purge gases with a flow rate of 170 mL min^{-1}. The furnace was left to cool down naturally to room temperature.

Two polymeric precursor films were prepared and carbonized according to temperature history #1, under a nitrogen atmosphere. The CMSM prepared with no additives was named CM0H11 (reference

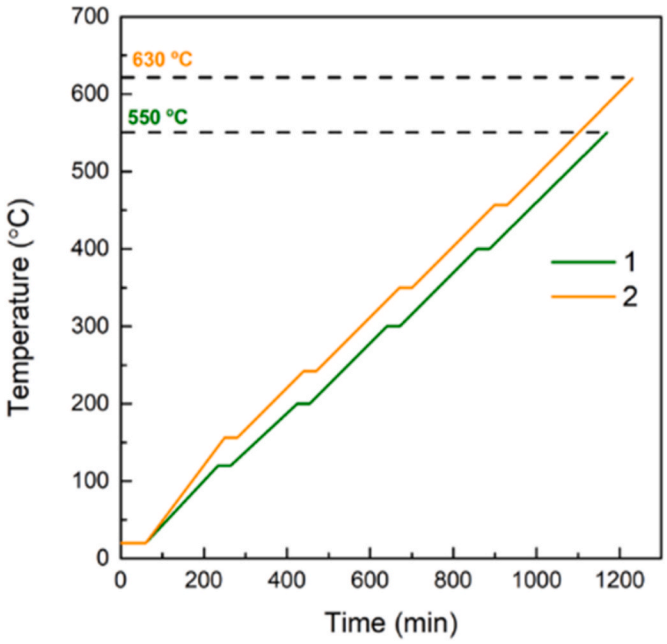

Fig. 3. Temperature histories considered in this work for preparing the CMSM.

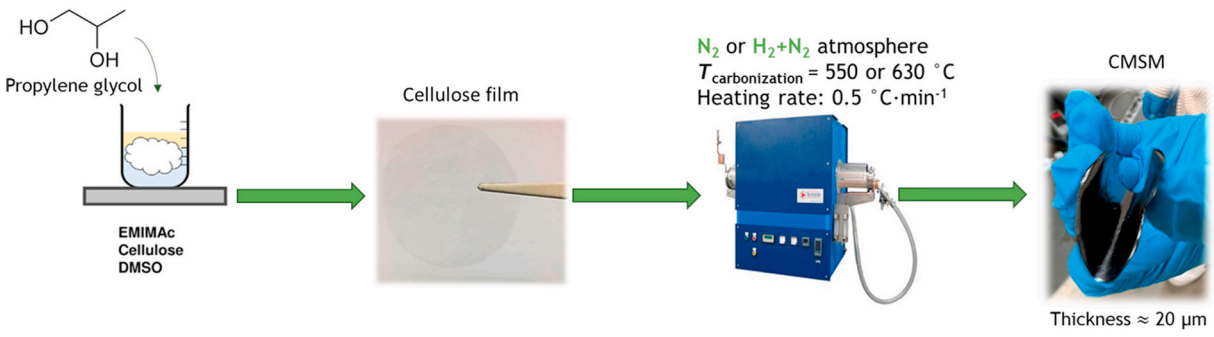

Fig. 2. Sketch of the cellulose-based CMSM fabrication applied in this work.

membrane), and the CMSM prepared with 1 wt% of propylene glycol was named CM1H11 – the nomenclature used to name each CMSM is explained in Table 1. In this work, the glycerol and urea were also added directly to the cellulose solution instead of using it in a softening bath. A carbonization atmosphere containing 5 % hydrogen balanced with nitrogen was used during the carbonization of membrane CM1H21. As a purge atmosphere containing H_2 makes the pores of the CMSM larger, a new carbonization history, with a higher end-temperature of 630 °C was applied to membrane CM1H22. A fifth membrane, named CM0H22, was prepared without propylene glycol but using temperature history #2 and carbonized under a flow atmosphere of 5 % of hydrogen balanced with nitrogen. Table 1 summarizes the preparation conditions of the membranes.

2.3. Gas permeation experiments

The single gas component experiments were performed using the time-lag method as described elsewhere [32]. The membrane permeability to gas *i*, L_i, was calculated by the time derivative of the permeating pressure, equation (1), assuming ideal gas behavior:

$$L_i = \frac{2.69 \times 10^{-3}\ \delta\ V}{T\ A_M\ (p_f - p_p)} \bullet \left[\left(\frac{dp}{dt}\right)_{\text{experiment}} - \left(\frac{dp}{dt}\right)_{\text{leak}} \right] \quad (1)$$

where δ is the membrane thickness, V is the volume of the permeate tank, T is the absolute temperature, p_f and p_p are the feed and the permeate pressures, respectively, and t is the time. The "leakage" rate of the experimental setup was determined before each membrane characterization for each gas. To determine the "leakage" rate, the set-up was pressurized to 2 bar, and the depressurization rate determined during *ca.* 24 h; the "leakage" was always $<10^{-4}$ Pa s^{-1}. The permselectivity, $\alpha_{i,j}$, of the CMSMs, was calculated from the permeability ratio of gas species *i* and *j*. The Robeson Index was also computed for each membrane and for each separation [38]. The gas permeability was expressed in barrer (1 barrer $= 3.39 \times 10^{-16}$ mol m m^{-2}•s^{-1} Pa^{-1}).

The permeabilities to H_2 and N_2 using humidified streams were determined for CM0H22, as a fresh membrane and after 60 days of aging in ambient lab conditions. To perform these experiments, the probing gas was bubbled through a column filled with distilled water, and the humidified gas was fed to the membrane cell. The relative humidity was determined using a dew-point meter (Vaisala DMP74b), as described elsewhere [28]. The permeabilities of the CMSM were determined for different temperatures, from 25 to 60 °C. The Arrhenius and the Van't Hoff equations were used to describe the dependence of diffusivity (D) and of sorption (S) coefficients, respectively, with the temperature [29]. The permeability can be written as the product of the diffusivity by the sorption coefficient ($L = D \times S$), assuming the sorption-diffusion model. The permeability as a function of the temperature can then be written as [29]:

$$L = D_0 \cdot e^{-\frac{E_{\text{diffusivity}}}{RT}} \times S_0 \cdot e^{-\frac{E_{\text{sorption}}}{RT}} = L_0 e^{-\frac{E_p}{RT}} \quad (2)$$

where L_0 is the pre-exponential factor and E_p is the apparent activation energy ($E_p = E_{\text{diffusivity}} + E_{\text{sorption}}$). The apparent activation energy for H_2, CO_2, N_2 and CH_4 were determined from the linear regression of the $\ln L$ *vs* $1/T$.

Table 1
Preparation conditions of the synthesized membranes. The generic name of the membranes is CM*x*H*yz*, where x = 0 means no additives and $x = 1$ means 1 wt% of propylene glycol; $y = 1$ means a purging atmosphere of N_2 and $y = 2$ means a purge atmosphere containing 5 % H_2 balanced with N_2; $z = 1$ refers to temperature history #1 and $z = 2$ refers history #2, as illustrated in Fig. 3.

	Precursor	Gas	Temperature history
CM0H11	No additive	N_2	1
CM1H11	1 wt% propylene glycol		1
CM1H21		N_2 + 5 % H_2	1
CM1H22			2
CM0H22	No additive		2

2.4. Carbon membrane and precursor structural and chemical characterization

The thermogravimetric analysis (TGA) of the cellulose precursors with and without propylene glycol were characterized in a NETZSCH STA 449 F3 Jupiter thermogravimetric balance under nitrogen flowrate of 30 mL min^{-1}, from room temperature until 600 °C, with a heating rate of 10 °C•min^{-1}. The precursor films were analyzed by FTIR in ATR mode using a VERTEX 70 FTIR BRUKER spectrometer with a high sensitivity DLaTGS detector from 4000 to 400 cm^{-1} with a resolution of 4 cm^{-1}. The morphology of the precursor films and of CMSMs were analyzed using a SEM microscope – Hitachi TM4000 plus (Hitachi, Tokyo Japan). The precursor films and CMSMs thickness was determined using a high-accuracy digital micrometer, Mitutoyo MDH-25 M, and confirmed by SEM. TEM micrographs of CMSM samples were analyzed on a JEOL-JEM-2100-HT microscope operated at 200 kV and equipped with a high-brightness LaB6 electron gun and a 4k x 4k CCD camera.

The crystallinity degree (I_{cryst}) of the precursor samples and the respective CMSM were characterized by x-ray diffraction (XRD) using a Rigaku SmartLabSe diffractometer (Cu Kα radiation – 1.5406 Å, 40 kV, 30 mA). The XRD patterns were collected in the range of 2θ from 7° to 60° with a step size of 0.017°. The interlayer distance (d-spacing) of the diffraction peaks was calculated using the Bragg equation. Raman spectra of the CMSMs were obtained using a WITEc alpha300 R Confocal Raman with an excitation wavelength of 532 nm. The CMSM samples were also analyzed by XPS – Kratos AXIS Ultra HAS using a monochromatic Al Kα X-ray source (1486.7 eV) at an operating voltage of 15 kV (90 W) in FAT mode (Fixed Analyzer Transmission). The pass energy was set at 40 eV for specific regions and 80 eV for the survey. The XRD, Raman and XPS peaks were analyzed by CasaXPS software.

The microporosity of the CMSM samples were characterized based on the adsorption equilibrium isotherm of CO_2 at 273 K (obtained by the volumetric method as described elsewhere in Refs. [31,32,39]) and the Dubinin-Raduschkevisch (DR) equation was fitted to the experimental data [40]:

$$\frac{w}{w_0} = \exp\left[-\left(\frac{RT \ln p_0/p}{\zeta E_0} \right)^2 \right] \quad (3)$$

where w is the micropore volume, w_0 is the total micropore volume, E_0 the characteristic adsorption activation energy, p is the pressure, p_0 is the vapor pressure of the free liquid, ζ is the affinity constant, R is the gas constant and T is the absolute temperature. The mean micropore size, ℓ_0, was computed using the Stoeckli equation, and the total surface area of micropores, S_{mic}, was calculated as follows [41,42]:

$$\ell_0 = \frac{10.8}{E_0 - 11.4} \quad (4)$$

$$S_{mic} = \frac{2000\ w_0}{\ell_0} \quad (5)$$

Micropore size distribution (MSD) of the prepared CMSM was obtained using the method proposed by Nguyen for the determination of the MSD in carbonaceous materials [43–45].

2.5. Simulation of the CMSM process for hydrogen recovery

The partial recovery of hydrogen from a medium-pressure (20 bar) natural gas pipeline containing 10 % hydrogen was simulated, as sketched in **Fig. 4A**. The operating temperature of the process was assumed constant and equal to the room temperature. As other authors

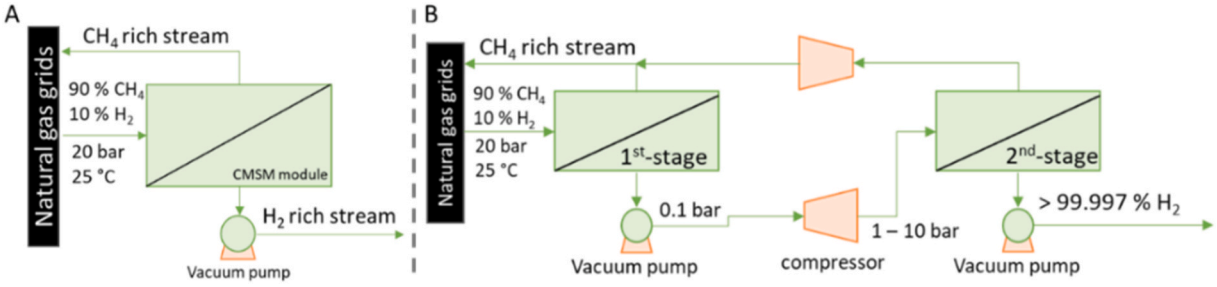

Fig. 4. Recovering hydrogen from natural gas networks using a single CMSM stage (A) and using a two CMSM stages (B).

had reported, a permeating hydrogen purity >99.7 % (Type I, Type II Grade D - ISO standard 14687-2) requires the use of more than one membrane stage (Fig. 4B). This present study considers a two-stage CMSM system for recovering *ca.* 80 kg of H_2 per day with a purity >99.997 % with approximately 95 % recovery – retentate hydrogen concentration of *ca.* 0.5 %. The conditions used in modeling the two hydrogen recovery systems are indicated in **Table 2**.

A counter-current membrane separation model was developed based on the main assumptions presented in Supplementary Note 2. The developed simulator considers the discretization of the domain in n equal perfectly mixed volumes. In this work, the set of differential equations is simultaneously solved in steady-state conditions using the function *solve_bvp* of Python™. To the best of the authors' knowledge, this is the first time a membrane counter-current model has been reported using the libraries of the Python programming language.

The outputs of the performed simulations are the hydrogen concentration and stage cut (θ). The specific membrane area (φ) is the ratio between the CMSM area and the feed flow rate. The stage cut is the ratio between the permeate flow rate and the feed flow rate. The stage cut is directly related to the recovery. The equations needed for the economic analysis are present in Supplementary Note 2 and reported elsewhere [47–50]. In this economic model, the specific cost of recovering hydrogen from natural gas grids ($€\cdot kgH_2^{-1}$ recovered) is calculated based on the ratio of the sum of the annual amortization cost of capital costs (C_{ACRC}) to the operating costs by the hydrogen recovered annually equation (5.6):

$$\text{Purified } H_2 \text{ specific cost } \left(€ \bullet kgH_2^{-1}\right) = \frac{C_{ACRC} + C_{OPEX}}{Q_{H_2}} \quad (5.6)$$

where, Q_{H_2} is the hydrogen permeate flow rate. The C_{ACRC} refers to the annual amortization of capital expenditures (CAPEX) – the amortization of the costs of equipment and system components is generally executed during the accomplishment of this type of project (5 years). The CAPEX for this simulation process was the sum of the cost of compressors, vacuum pumps, and membrane modules (a membrane cost of 100 $€\cdot m^{-2}$ was assumed as has been reported by other authors for CMSM [46,47, 50]), and a rate of 20 % is considered for non-dimensioned equipment. The CAPEX was updated with the chemical engineering plant cost index (CEPCI) of 699.97 (2021) for the equipment adopted for all inflation adjustments of 397 (*I*). For the operational-related expenditure costs (OPEX – C_{OPEX}) only the electricity cost used for compressors and vacuum pumps was considered, with an electricity price of 0.08 $€\cdot kWh^{-1}$. The labor, maintenance costs, and other utility costs were neglected since they have a negligible weight in the cost compared to energy consumption. The plant time operation was assumed to be 8000 h per year.

Table 2
Membrane separation conditions and parameters used to model the H_2 recovery from a natural gas network.

Parameter	Scenario 1	Scenario 2	Scenario 3
Feed gas flow rate, $mol\cdot s^{-1}$	5–450	5	5
Feed pressure, bar	20	20	20
Feed pressure (2nd stage), bar	–	optimized	optimized
Permeate pressures, bar	0.1	0.1	0.1
Gas composition, (H_2:CH_4) %	10:90	10:90	10:90
H_2 permeance[a], $mol\cdot m^{-2}\cdot s^{-1}\cdot Pa^{-1}$	5.5×10^{-8}	5.5×10^{-8}	1.3×10^{-7}
CH_4 permeance[a], $mol\cdot m^{-2}\cdot s^{-1}\cdot Pa^{-1}$	1.1×10^{-11}	1.1×10^{-11}	1.2×10^{-10}
H_2 productivity, $kg\cdot day^{-1}$	–	>80	>80
H_2 purity, %	–	>99.997	>99.997
Retentate H_2 concentration, %	–	<5	<5

[a] The permeances were calculated assuming a selective membrane thickness of 3 μm as reported by other authors [29,46,47].

3. Results and discussion

3.1. Carbon membrane gas separation performance

The prepared CMSMs were characterized concerning the permeability to 4 target gases, H_2 (kinetic diameter = 0.290 nm), CO_2 (0.335 nm), N_2 (0.378 nm), and CH_4 (0.380 nm) under a dry basis stream. Fig. 5A plots the permeabilities of membranes CM0H11, CM1H11, CM1H21 as a function of the kinetic diameters of the permeating gas, while Fig. 5B plots the permeabilities of membranes CM1H21, CM1H22, CM0H22. Table S1 from the Supplementary Note 1 shows the obtained permeability, selectivity, and respective Robeson Index values.

The membrane CM0H11 was prepared with no additives and carbonized under a nitrogen atmosphere, and it serves here as the reference membrane. The membrane performance to separations H_2/CH_4, H_2/N_2, and H_2/CO_2 show Robeson Indexes greater than 1, indicating that the separation performance of this CMSM is above the referred Robeson upper bound [38].

Membrane CM1H11 was prepared by adding propylene glycol to the cellulose precursor solution. The H_2/CO_2, H_2/N_2 and H_2/CH_4 selectivities of this membrane are higher than for the reference membrane, respectively 11.6 *vs.* 4.9; 808 *vs.* 254 and; 3498 *vs.* 684; it should be emphasized the increase of 5x concerning the separation H_2/CH_4.

The permeability of CM1H11 to hydrogen was not impaired compared to the reference membrane, allowing to obtain a 5 times improvement of the Robeson Index, from 19 to 100. Propylene glycol narrowed the pore size distribution, making the permeation more difficult for the bulkier molecules without hindering the permeation to hydrogen. Compared to introducing the propylene glycol additive in the cellulose solution or introducing it in the coagulation bath, the results are similar; however, introducing the propylene glycol additive in the cellulose solution makes the procedure easier [31]. Other authors observed similar improvements with other additives, such as glycerol [34]. The results of incorporating 2 wt% of propylene glycol, 1 wt% of glycerol, and 1 wt% urea can be found in Table S2 Supplementary Note 1.

Membrane CM1H21 was prepared, introducing 5 vol% of hydrogen, balanced with nitrogen, in the carbonization atmosphere. The obtained results show that the permeability of CM1H21 to all the tested gases increased – Fig. 5A. An increase of *ca.* 42 % was obtained in the permeability of the CMSM to hydrogen, displaying now a permeability

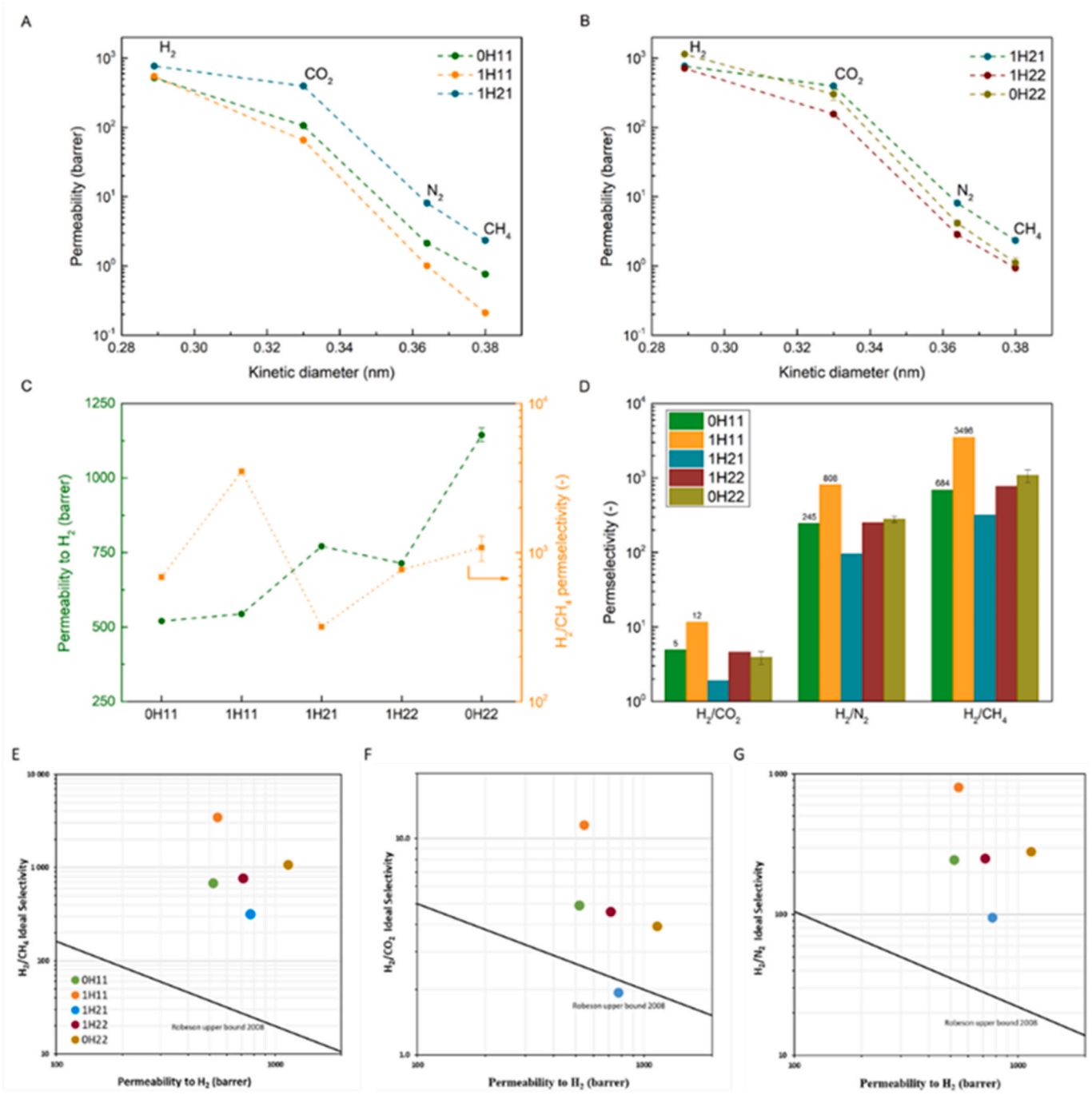

Fig. 5. (A) and (B) plot the permeability as a function of the gas kinetic diameter for all the prepared carbon membranes. (C) plots the permeability to H_2 and H_2/CH_4 permselectivity as a function of the prepared carbon membranes; (D) displays the permselectivity of the fabricated carbon membranes to the gas separations. Robeson plots for H_2/CH_4 (E), H_2/CO_2 (F) and H_2/N_2 (G) separations. Interrupted lines were added to guide the eyes.

of 771 barrer. However, the permeability to bulkier gases also increased, *e.g.* the permeability to CO_2 increased six times, from 66 barrer to 396 barrer, leading to the reduction of the selectivities and the corresponding Robeson Indices for all gas separations. The membrane CM1H22 was carbonized to 630 °C of end temperature – temperature history #2 – to increase the selectivity for hydrogen separations compared with membrane CM1H21. Fig. 5B shows that the permeability of membrane CM1H22 to hydrogen is mostly the same as for membrane CM1H21, but all selectivities increased noticeably; namely, the Robeson Index for the H_2/CH_4 separation doubled from 13 to 29.

Membrane CM0H22 was carbonized as CM1H22 but without adding propylene glycol. Interestingly, this new membrane displayed the highest permeability to H_2, 1144 barrer, while the selectivities were kept constant or increased. This is the case of H_2/CH_4 selectivity that increased from 768 to 1080, with the Robeson index increasing from 29 to 62. In Fig. 5C, the permeability to H_2 and H_2/CH_4 selectivity are plotted as a function of the prepared membranes. This figure summarizes the performance of the prepared membranes to the different gas separations. Fig. 5E–G plot all the results; except for one case, the performance of all membranes to all gas separations display is above the Robeson upper bound.

3.2. Cellulose-based precursor characterization

The thermogravimetric (TGA) plots of the polymer precursor films with and without propylene glycol – CM0H and CM1H – are shown in Fig. 6A. Both TG curves show four distinct zones, in agreement with the literature [34]. The first zone, up to *ca.* 150 °C, corresponds to the removal of water trapped in the polymer and other volatile species. The sample containing propylene glycol displays a higher mass loss; most of the mass loss should be assigned to the hygroscopic nature of propylene glycol (boiling point of 188.2 °C), which makes the cellulose film retain more water molecules that leave during the first TG zone. The mass loss that occurs in the second zone, between 150 °C and 250 °C, is smaller and similar for both curves.

The mass loss observed in the third zone, between 250 °C and 340 °C, corresponds to the on-set of cellulose matrix decomposition with the formation of the pore network; finally, in the fourth zone, above 340 °C, further degradation of the cellulose occurs, the pore network begins to organize itself and the carbon matrix compacts. From the derivative of the mass loss curves (DTGA) it was possible to determine that the onset of decomposition temperature of the cellulose matrix is higher for the precursor prepared without additive. Furthermore, a higher mass loss is observed for the precursor prepared with propylene glycol (14.9 %). The TG results are displayed in Table 3.

The crystalline structure of the prepared precursors was assessed using X-ray diffraction (XRD), and the results are presented in Fig. 6B. The characteristic planes of cellulose II were observed in both cellulose precursors. The peaks are located at 2θ *ca.* 12°, 20° and 21°, which correspond to planes (1 $\bar{1}$ 0), (110) and (020), respectively [51,52], likewise observed in our previous work with urea [32]. From the XRD patterns it is possible to detect a decrease on the plane (1 $\bar{1}$ 0) and an increase on the plane (110), indicating a greater reorganization of the crystalline structure of the prepared polymeric precursor. The crystallinity index (I_{Cryst}) of the polymer precursor increases from *ca.* 31 to 43 %, showing that the propylene glycol can increase the crystallinity of the cellulose matrix, which should happen because an increase in van der Waals forces, as reported by Fauziyah et al. [53]. Propylene glycol delays the drying of the cellulose film allowing a better compaction of the cellulose chains and an increase in crystallinity.

Table 3
Thermal and structural characterization of polymeric cellulose precursors prepared.

	No additive	1 wt% MPG
Onset of the decomposition temperature (°C)	342.5	332.8
Mass loss at 150 °C (%)	11.0	14.9
Residual mass at 550 °C (%)	22.2	17.3
Residual mass at 630 °C (%)	21.1	9.7
Crystallinity index (I_{Cryst}) (%)	30.9	42.9

FTIR spectra were used to assess the effect of the propylene glycol presence on the chemical structure of the prepared cellulose precursors. The FTIR spectra are shown in Fig. 6C. This analysis indicates that propylene glycol did not introduce new functional groups or new chemical bonds in the sample. The bonds depicted in Fig. 6C are characteristic of polymeric precursors fabricated from cellulose regenerated using an ionic liquid (Emimac:DMSO) [28,29].

Scanning electron microscopy (SEM) was used to study the surface and cross-section of prepared precursors. Surface and cross-sectional SEM images of precursor prepared with and without additive are shown in Fig. 6D–G. The surface morphology of the prepared precursors is similar. Regarding the cross-section, the film prepared with propylene glycol has a thickness of *ca.* 29 μm, and the sample without propylene glycol has a thickness of 35 μm. This difference in thicknesses may be due to the lower viscosity of the polymeric precursor solution containing propylene glycol.

3.3. Structural and chemical characterization of the prepared CMSM

SEM images of the surface and cross-section of the prepared CMSMs are presented in Figs. S1A–E from Supplementary Note 3. The surface chemistry of the prepared CMSMs was analyzed by XPS and the C1s and O1s spectra are presented in Fig. 7A–B, respectively. The C1s and the O1s spectra of the carbonized polymeric precursors were deconvoluted

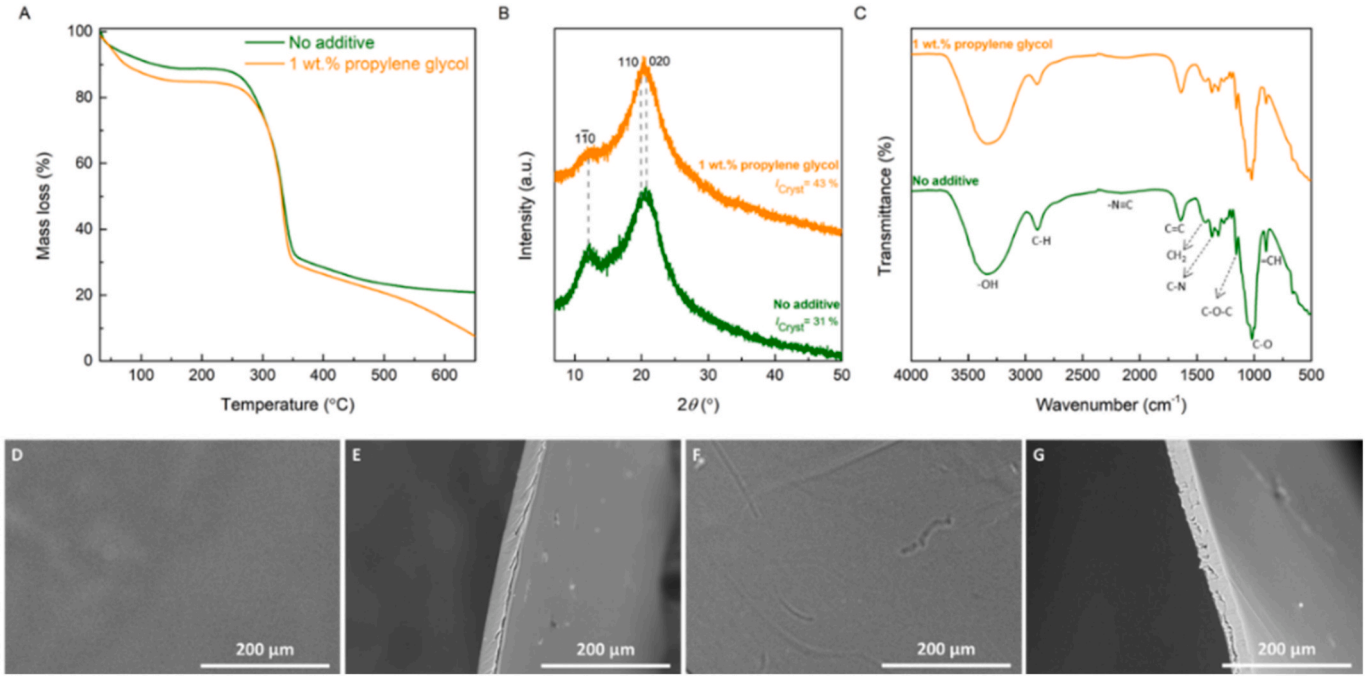

Fig. 6. (A) TGA curves performed under a nitrogen flow atmosphere of the cellulose films prepared with and without propylene glycol additive; (B) XRD patterns of the cellulose films and (C) FTIR spectra of the cellulose films. SEM images of the surface and cross-section of the cellulose films prepared with no additive (D) and (E) and with propylene glycol additive (F) and (G) - magnification: x200.

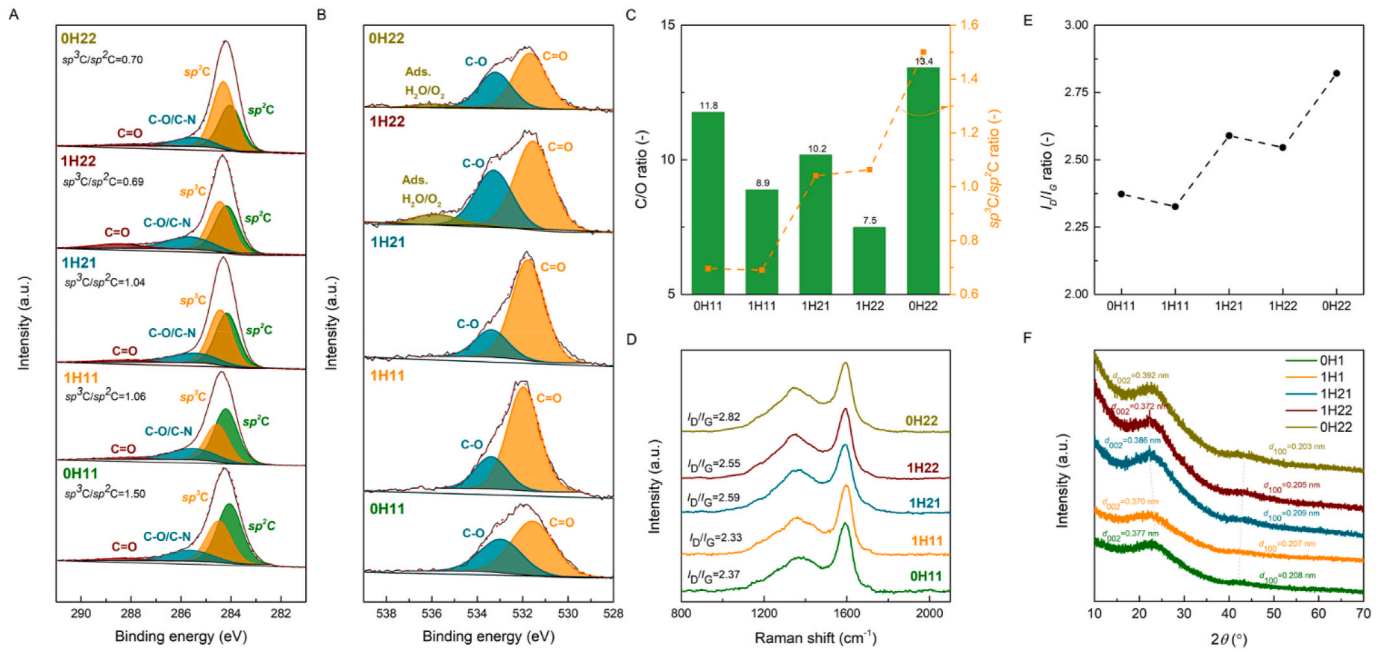

Fig. 7. XPS spectra of (A) C1s and (B) O1s with respective deconvoluted peaks for the different CMSM; (C) Influence of the C/O and sp^3C/sp^2C determined by the XPS on the prepared CMSM; (D) Raman spectra; (E) Influence of the I_D/I_G; (F) XRD diffractogram with the respective *d*-spacing.

and peak fitted to Gaussian-Lorentzian peak shape functions using the CasaXPS software. Shirley-type background were used and the binding energies (BE) were referenced to the C 1s line at 285 eV from adventitious carbon (Supplementary Note 4) [54]. From the C1s XPS spectra it is possible to see four characteristic bonds. CMSMs present a hybrid structure comprising sp^2 and sp^3-hybridized carbon, as reported elsewhere [29,55]. The samples prepared in this work present two distinct peaks: one located at 284 eV BE assigned to the sp^2-hybridized carbon, and another peak located at *ca.* 285 eV, which can be attributed to the sp^3-hybridized carbon. The peaks located at *ca.* 286 eV, were assigned to C–O and C–N bonds, and the peak located at 289 eV was assigned to the C═O [56]. The sp^3-hybridized carbon bond is responsible for forming micropores, *i.e.*, imperfect packing of the graphite plates, as reported elsewhere [55]; and from Fig. 7A it is possible to observe that the addition of propylene glycol produced a membrane – CM1H11 – with a more organized structure (less sp^3-hybridized carbon) originating a slight decrease in the sp^3/sp^2 ratio; and, as first reported by Ma et al. [37], with the introduction of H_2 into the carbonization atmosphere, the sp^3/sp^2 ratio increases considerably due to the highest disorder and lowest packing density of the graphite sheets; however, when the end carbonization temperature was increased, this ratio remained almost constant (1.04 for CM1H21 and 1.06 for CM1H22, respectively). The sp^3/sp^2 ratio seems to justify the non-variation of the permeability to hydrogen of CM1H22, and as expected, CM0H22 presents the highest sp^3-hybridized carbon fraction and the highest sp^3/sp^2 ratio indicating that this membrane should present a higher permeabilities due to its higher porosity (lower carbon packing density – higher porosity).

Fig. 7B shows the XPS O1s spectra with the characteristic peaks appearing at *ca.* 531 eV, corresponding to C═O binding, while the second peak, at *ca.* 533 eV, corresponds to C–O binding [30]. From the analysis of the XPS O1s spectrum, it is possible to see that the membranes prepared with propylene glycol (CM1H11, CM1H21, and CM1H22) present the most pronounced C═O specific band. Additionally, the characteristic peak of adsorbed water and oxygen appears in the CM0H22 and CM1H22. The presence of this peak indicates that these CMSMs are susceptible to oxygen chemisorption aging, as reported elsewhere [31].

The C/O ratio was determined was also determined by XPS. This parameter is indicative of the number of oxygenated groups on the surface of the prepared membranes; low C/O ratios are indicative of lower permeabilities and higher selectivities, as reported elsewhere [31]. Fig. 7C, shows the C/O and the sp^3/sp^2 ratios of all the prepared CMSMs. A decrease in the C/O ratio is observed in CM1H11; when H_2 was added to the purging atmosphere, less oxygenated groups were formed. Therefore, CM0H22 has the highest C/O ratio but also has the highest sp^3/sp^2 ratio, this being the CMSM with the best separation performance – high permeabilities and high selectivities for separations of small gases from bulkier gases (*e.g.* H_2/CH_4).

Fig. 7D displays the Raman spectra used to analyze the crystallinity of graphite platelets of the prepared CMSMs. A typical spectrum of carbon has two very characteristic peaks: the G peak, located *at ca.* 1600 cm^{-1} and related to the vibrational mode of the sp^2-hybridized carbon bonds (E_{2g}-simmetric); and the peak D, at *ca.* 1350 cm^{-1}, assigned to the vibrational mode of disordered graphite (A_{1g}-symmetry) [57,58]. These two peaks are present in all the prepared carbon membranes. These two peaks were deconvoluted using the OriginPro software in Gaussian (peak D) and Lorentzian (Peak G) to determine their areas to calculate the I_{D1}/I_G ratio. It is known that a higher area of peak D indicates more defects in the carbon matrix and then a higher permeability (Table S9 – Supplementary Note 4). Fig. 7E shows the I_{D1}/I_G ratio values of the prepared membranes, and as expected, the trend of this curve is identical to that of the sp^3/sp^2 ratio, where the lowest I_{D1}/I_G value corresponds to the membrane with the highest selectivity. Propylene glycol makes the carbon structure more graphitic, the opposite of when urea is added [32]. CM0H22 has an I_{D1}/I_G value of 2.82, indicating that this sample presents a superior disorder of the carbon platelets.

Fig. 7F displays the diffractograms of the prepared CMSMs samples. CMSMs present a turbostratic carbon structure with a graphite plate imperfectly packed; this makes its structure mostly amorphous. The XRD diffractograms of carbon membranes show the plane (002), located at $2\theta \approx 24.6°$ assigned to the graphitic domains (sp^2 carbon); and the plane (100) located at $2\theta \approx 42.6$. The interlayer distance (*d*-spacing) of the CMSMs was calculated, and the respective *d*-spacing of the different carbon plates is shown in the figure. The XRD diffractograms were treated in the Origin Pro software, deconstructing the characteristic peaks of these two planes in two Gaussian curves. The *d*-spacing is not a measure of the porosity of the membranes, but it can indicate the average distance of the planes (002). CM1H11 has the lowest *d*-spacing

(0.370 nm) and is also the carbon membrane with the highest selectivities. The membrane with the highest permeabilities, CM0H22, has the largest *d*-spacing, and it is also this CMSM that has the highest sp^3/sp^2 ratio. Table S10 from the Supplementary Note 5 summarizes the XPS, Raman, and XRD results, demonstrating that the parameters evaluated by these characterization techniques are consistent with the permeability and selectivity results of the produced CMSM.

TEM micrographs are a powerful tool to assess the atomic morphology of the carbon matrix. Two TEM micrographs are shown in Fig. 8A–B for membranes CM1H11 and CM0H22, respectively. These two membranes were selected because membrane CM1H11 is the reference, and membrane CM0H22 displays the best separation performance. Comparing the two micrographs, it is possible to observe that CM1H11 sample (Fig. 8A) presents more aligned chains and a more ordered structure, characteristic of carbon materials with more sp^2-hybridized carbon as verified in XPS and lower *d*-spacing and lower I_{D1}/I_G ratio as verified in Raman, therefore, superior selectivities are expected. Inversely, membrane CM0H22 (Fig. 8B), presents a less ordered carbon structure, corroborating the remaining morphological characterization techniques presented before.

3.4. Microporosity and pore size distribution analysis

The CMSM microporosity was assessed based on the carbon dioxide adsorption equilibrium isotherms at 0 °C, Fig. 9A. The CO_2 adsorption equilibrium isotherms were determined by the volumetric method. This technique allows to determine the volume and distribution of micropores larger than the size of the CO_2 molecule [28]. The adsorption capacity at 1.3 bar presents the highest value for CM0H22, which is also the membrane with the highest permeability to CO_2. The trend in adsorption capacities agrees with the permeability results and follows the following order: CM0H22 > CM1H22 > CM1H21 > CM0H11 > CM1H11. In this work, the Dubinin- Raduschkevisch equation was fitted to the experimental data, and the micropore volume, w_0, and the characteristic energy, E_0, were determined. Using equations (4) and (5), the mean pore size (ℓ_0) and the total surface area of the micropores (S_{mic}) were also computed. The volume of the micropores and the mean pore size are shown in Fig. 9B. All results of the micropore analysis are summarized in Table 4.

The results presented in Table 4 are typical for carbon membranes produced from cellulose precursors [28,29,34]. Fig. 9B shows the volume of the micropores and the mean pore width for the prepared CMSMs. It can be concluded that adding propylene glycol promotes the reduction of the volume of the micropores and of the mean pore size, which agrees with the gas permeation results; conversely, adding H_2 to the carbonization flow atmosphere induces an increase in the volume of the micropores from 0.308 to 0.380 $cm^3 \cdot g^{-1}$; while the modification in the carbonization temperature history barely changes the volume of the micropores, corroborating the results obtained in the previous sections. This work reports, to the best knowledge of the authors, the largest micropore volume of a cellulose-based carbon membrane, namely CM0H22, with a micropore volume of 0.443 $cm^3 \cdot g^{-1}$. The preparation conditions of membrane CM0H22, compared with reference membrane CM0H11, allowed to increase the volume of the micropores from 0.356 to 0.443 $cm^3 \cdot g^{-1}$, while keeping the mean micropore size mostly constant, 0.661 nm *vs*. 0.667 nm, respectively. Regarding the total internal surface micropores area, it follows the same trend as the volume of micropores, 1326 $m^2 \cdot g^{-1}$ for CM0H22 compared with 1079 $m^2 \cdot g^{-1}$ for CM0H11 membrane.

The micropore size distribution (MSD) was determined, using the method developed by Nguyen for microporous carbonaceous materials [43–45]. A bimodal pore size distribution was obtained for all samples. Fig. 9C shows the micropore size distributions of CM0H11, CM1H11, and CM1H21 membranes. As expected, propylene glycol shifted the micropore size distribution to the left, *i.e.* to the region of smaller micropores, compared to the reference CM0H11 sample. Furthermore, CM1H11 shows no micropores wider than 0.9 nm. Adding a reducing agent (H_2) to the carbonization atmosphere widened the pores – *cf*. Fig. 9C, sample CM1H11 *vs*. CM1H21. On the other hand, increasing the carbonization end temperature – temperature history #2, increased the volume fraction of pores within 0.4–0.55 nm, making the distribution more bimodal. Membrane CM0H22 shows a high-volume fraction of micropores between 0.6 and 0.9 nm and the highest volume fraction between 0.45 and 0.55 nm, which seems to agree with the obtained permeation results.

3.5. Separation performance of the CMSMs under different operating conditions

In this section, the stability of the separation performance of the CM0H22 membrane is evaluated. The effect of oxygen chemisorption, the temperature effect, the effect of feed pressure, and the separation stability in the presence of humidified gases is studied.

3.5.1. CM0H22 aging evaluation

Membrane CM0H22 was stored under lab atmospheric conditions to assess the stability of this membrane in the presence of ambient oxygen and humidity. Carbon membranes can be affected by irreversible oxygen

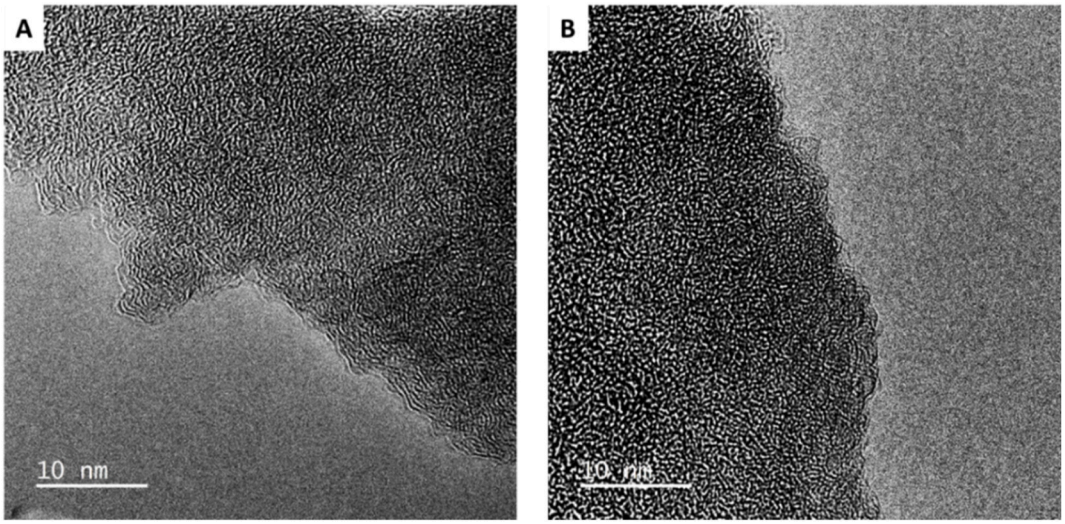

Fig. 8. TEM micrographs of (A) CM1H11 and (B) CM0H22.

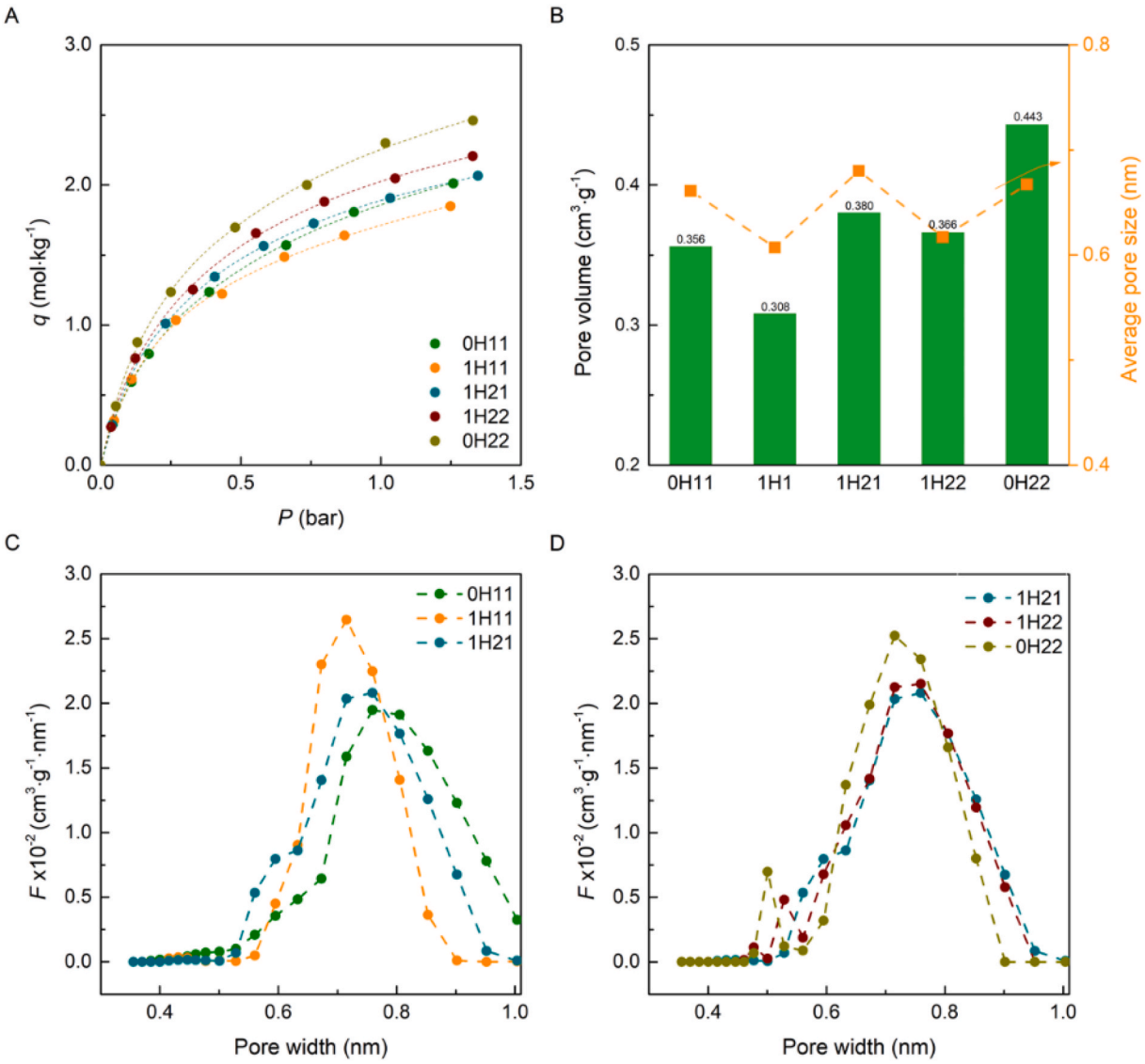

Fig. 9. (A) Carbon dioxide adsorption equilibrium isotherms determined at 0 °C for all the carbon membranes prepared in this work; (B) computed micropore volume and mean pore size determined from the DR and Stoeckli equations; (C–D) Micropore size distribution of the fabricated CMSMs. Lines were added to guide the eyes.

Table 4
Micropore structural characterization based on the parameters from the DR equation fitted to CO_2 adsorption isotherms at 0 °C.

	w_0 ($cm^3 \bullet g^{-1}$)	E_0 ($kJ \bullet mol^{-1}$)	ℓ_0 (nm)	S_{mic} ($m^2 \bullet g^{-1}$)
0H11	0.356	27.8	0.661	1079
1H11	0.308	29.2	0.607	1016
1H21	0.380	27.3	0.680	1116
1H22	0.366	28.9	0.617	1187
0H22	0.443	27.6	0.667	1326

chemisorption when exposed to ambient conditions [36]. After 30 days in lab ambient conditions, the permeability of membrane CM0H22 to H_2 dropped from 1123 to 1021 barrer, this reduction (*ca.* 10 %) is lower than usually observed with similar membranes; for example, Lei et al. [29] reported a *ca.* 33 % reduction in the permeance to hydrogen. Regarding the H_2/CH_4 permselectivity, it was observed an increase of *ca.* 18 %. The same membrane was aged for more 30 days under the same conditions (60 days in total); the permeability to H_2 dropped by almost 40 %, to 677 barrer, and the H_2/CH_4 permselectivity increased to 2095 (Table S11 – Supplementary Note 6). Anyway, CMSMs are fully stable when working under a reducing atmosphere, such as mixtures of methane and hydrogen. Also, they can be made stable if, after the carbonization stage, they are immersed in a propylene atmosphere for a period of time, as reported elsewhere [31].

3.5.2. *Temperature effect on the gas permeation*

A fresh CM0H22 sample (sample #2), after 50 days of aging in ambient air conditions, was tested at several different temperatures, 25 °C, 35 °C, 45 °C, and 60 °C. The CMSM permeability to H_2, CO_2, N_2, and CH_4 and the respective permselectivities H_2/CH_4, H_2/N_2, and H_2/CO_2 were obtained and plotted in Fig. 10A–C as a function of the temperature. It can be observed that the temperature has a large effect on the permeability of CM0H22. The permeability of CM0H22 to hydrogen at 25 °C is 529 barrer increasing to 1378 barrer at 60 °C. Regarding the permeability of the membrane to methane, it increases from 0.32 barrer at 25 °C to 1.97 barrer at 60 °C, making the H_2/CH_4 selectivity to decrease 57 %. On the other hand, the permeability to CO_2, increased only slightly, from 80 to 172 barrer, making the H_2/CO_2 selectivity increase from 6 to 8. Finally, the H_2/N_2 selectivity decreases from 219 to 135 (Table S14 – Supplementary Note 9).

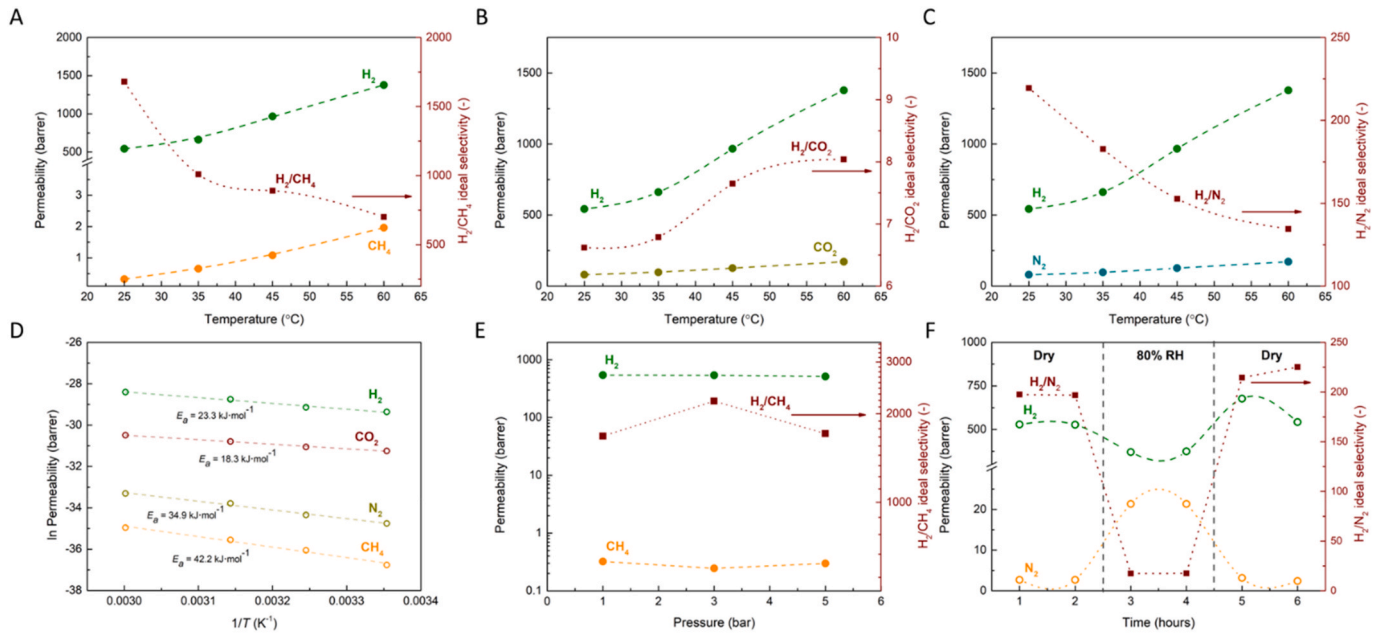

Fig. 10. Evaluation of the separation performance of CM0H22 aged for 50 days as a function of the permeability test temperature for mixtures (A) H_2/CH_4, (B) H_2/CO_2 and (C) H_2/N_2; (D) Arrhenius plots for all the tested gases of the CM0H22; (E) Variation of H_2 permeability and H_2/N_2 selectivity as a function of supply pressure; (F) Effect of feed gas relative humidity on the H_2/N_2 separation performance of CM0H22. Lines were added to guide the eyes.

Table S15 from the Supplementary Note 9 and Fig. 10D show the apparent permeation activation energy (E_p) for each gas studied. From the Arrhenius plots – Fig. 10D, it is possible to observe that E_p increases with the kinetic diameter of the gases, except for CO_2. The apparent activation energy follows the pattern $CO_2 > H_2 > N_2 > CH_4$. The activation energy can help to determine the size of micropores responsible for the molecular sieving [26]. As the pore size gets tighter, more energy is required for the gas molecule to permeate the pore. The E_p obtained for CO_2, leads us to conclude that the predominant separation mechanism is adsorption on the carbon membrane hydrophilic site. The sharp increase in the N_2 and CH_4 suggests that the pore sieving size is between the size of CO_2 and N_2 (respectively 0.33 nm and 0.36 nm). The combined effect of adsorption and molecular sieving can be observed with the methane molecule, as the E_p value obtained is very high (42.2 kJ mol^{-1}), suggesting that the methane molecule is adsorbing only on the larger micropores.

3.5.3. Feed pressure effect on the gas permeation

The CM0H22 permeability was used to study the effect of feed pressure on gas permeation. Three different feed pressures were considered: 1 bar, 3 bar and 5 bar, where the permeate side was under vacuum – 0.02 bar. The methane and hydrogen permeation results and their selectivity are shown in Fig. 10E. Within the experimental error, the permeabilities and selectivities are approximately constant (Table S13 – Supplementary Note 8).

3.5.4. Humidity effect on the gas permeation

A fresh sample of membrane CM0H22, sample #3, was aged for *ca.* 50 days under ambient lab conditions. Hydrogen and nitrogen were bubbled through a column filled with water to produce humidified gas streams. Cellulose-based carbon membranes were the first reported as having the ability of permeating humidified gas streams without pore blockage [36]. The gas permeation results are presented in Fig. 10F. The permeability to two gases is plotted, N_2 and H_2; first they are supplied dry, they humid (80 % RH) and last dry again. The permeability indicated for the humidified streams is the combined permeability to the permanent gas plus to the water vapor. Since the permeability to water vapor is higher than the permeability to N_2, the combined permeability is higher. On the other hand, since the permeability to H_2 is higher than that to water vapor, the combined permeability is lower than for dry H_2. After the humidified streams tests, the membrane permeability to H_2 and N_2 returned to their initial values before the humid test (Table S12 – Supplementary Note 7). These results indicate that membrane CM0H22 does block nor age in the presence of humidity.

3.6. Techno-economic analysis of H_2 deblending from natural gas

A detailed techno-economic analysis of hydrogen recovery from the natural gas grids was performed based on the separation metrics of the prepared CMSMs. Firstly, the influence of the specific membrane area (the ratio between the membrane area and the feed flow rate) in the H_2 purity and stage cut (ratio between the permeate flow rate and the feed flow rate) was studied in a single CMSM stage system. Moreover, the specific cost of the purified hydrogen was computed for four different feed flows. Fig. 11 presents the separation performance of the best membranes reported in the literature for separating hydrogen from natural gas networks (H_2/CH_4) [59,60]. The membranes prepared in this work display the best balance between permeability and selectivity (highest values of Robeson Index) [17,26,61–63].

The results of the H_2 concentration (purity) recovered using a single-stage CMSM and the stage cut as a function of the specific membrane area (the ratio between the membrane area and the feed flow rate) are shown in Fig. 12A. From this study, the highest H_2 concentration that can be recovered in a CMSM module (with a constant pressure ratio equal to 200) is 99.8 %. The H_2 concentration decreases when the CMSM area increases, and the H_2 concentration increases when the stage cut increases (which is directly related to the recovery). The economic analysis was carried out for 4 different feed flows (scenario 1), and the results of the specific cost of recovering hydrogen can be found in Fig. 12B. The specific cost of hydrogen purification decreases with the H_2 concentration increase until the nominal concentration is reached. The nominal hydrogen concentration, *ca.* 99.75 %, corresponds to the optimal result for this carbon membrane system, where the sum of the annual capital amortization and operating costs are minimal for a given flow rate of hydrogen collected in the permeate. The minimum hydrogen purification cost obtained was 0.26 €·kgH_2^{-1}, which

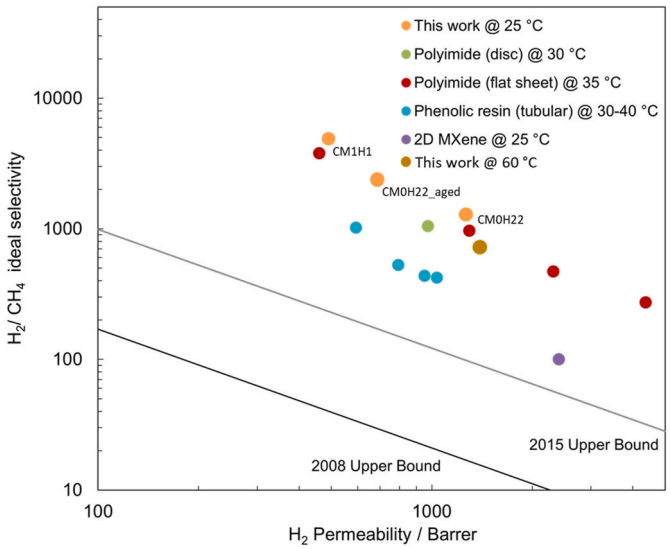

Fig. 11. H_2/CH_4 separation metrics of several membranes on the Robeson plot. A single-stage carbon membrane module equipped with membrane CM1H11 was assessed to recover hydrogen from a natural gas network. It was assumed that natural gas–hydrogen mixture has 10 % of hydrogen, and it is at 25 °C and 20 bar – Fig. 4A. The membrane driving force is guaranteed by a vacuum pump (0.1 bar) at the permeate side, and the retentate pressure was assumed to be 20 bar (feed-to-permeate ratio of 200).

corresponds to a feed rate of 450 mol s^{-1} with a CMSM area of 5000 m^2 and allows the production of 5866 $kgH_2 \cdot day^{-1}$ with a purity of 99.7 % and a hydrogen loss to the natural gas grid of 32 %.

High-grade hydrogen requires a minimum concentration of 99.997 %. In this work, a two-carbon membrane stage system was simulated – Scenario 2, Fig. 4B, for reaching this concentration. The second-stage feed pressure was optimized to ensure the minimum hydrogen-specific production cost. Vacuum was applied to the permeate side of both membrane modules; a pressurized feed was applied to the feed of the second stage module. The maximum hydrogen loss through the retentate was set to 5 % of the feeding hydrogen (hydrogen recovery of 95 %), and the production rate was set to 80 $kgH_2 \cdot day^{-1}$ – suitable to fill two Toyota Mirai hydrogen reservoirs. The results of optimizing the 2nd-stage feed pressure are shown in Fig. 13A–B. Higher hydrogen concentration (>99.997 %) can be reached using two membrane stages. As expected, the power demand increases with the feeding pressure to the 2nd stage – Fig. 13A.

The annual capital-related cost (ACRC) increases with the pressure ratio. Although the CMSM area decreases with the pressure ratio, the cost of the compressor has a significant impact on the CAPEX. As expected, the energy costs increase when feed pressure increases, increasing the OPEX – Fig. 13B. From this optimization, the lowest cost of purified hydrogen with the desired specifications is obtained at the lowest pressure ratio (1 bar feed pressure to 2nd stage). A purification cost of 1.88 $€ \cdot kgH_2^{-1}$ was computed to recover 83 kg of H_2 per day, with a concentration of 99.997 %, in a two-stage CMSM with an area of 460 m^2 and an energy consumption of 4.87 $kWh \cdot kgH_2^{-1}$.

A two-stage CM1H11 system with a feed rate of 450 mol s^{-1} was simulated and an extremely low H_2 purification cost of 0.32 $€ \cdot kgH_2^{-1}$ was obtained to recover hydrogen from the natural gas network with a concentration of 99.997 %.

The use of membrane CM0H22 (which displays a high permeability to hydrogen but a lower selectivity) in the hydrogen recovery and purification system of natural gas was also simulated in this work – Scenario 3. The operating conditions used for this simulation were the same as those in Scenario 2. In the first membrane stage, it was possible to recover 97.1 % of the hydrogen in an area of 100 m^2. The feed pressure to the second stage was 1 bar (optimum pressure, *cf.* previous section), and the area of the CM0H22 was optimized to meet the above-mentioned objectives: >95 % of H_2 recovery and a purity of >99.997 %. The results of this study are shown in Fig. 14A. The two-stage process using membrane CM0H22 could not reach the target hydrogen concentration and recovery. Because of the required high hydrogen purity, the lower selectivity displayed by membrane CM0H22 did not allow it to reach this milestone. Fig. 14A shows that the specific cost remains practically constant up to 99.994 % of purity – nominal concentration, increasing remarkably when the desired concentration is achieved.

Furthermore, a different configuration of a two-stage membrane system was simulated: the first stage used the membrane with higher H_2 permeability – membrane CM0H22 – followed by a second stage using the membrane with higher selectivity – membrane CM1H11; the same simulation conditions as in the previous sections were used. The results of this study are summarized in Fig. 14B. With this new design, it was possible to reach a hydrogen concentration of 99.996 % in the second stage with an area of 35 m^2 and a hydrogen recovery of 95.4 % – feeding hydrogen concentration of 10 % and retentate hydrogen concentration of 0.46 %. The obtained specific cost was 1.77 $€ \cdot kgH_2^{-1}$ – 6 % cheaper than using just membrane CM1H11. Table S16 from Supplementary Note 10 summarizes the key results of the simulations carried out.

This techno-economic analysis shows that two-stage CMSM can be used to recover H_2 from the natural gas grid with high recovery and high

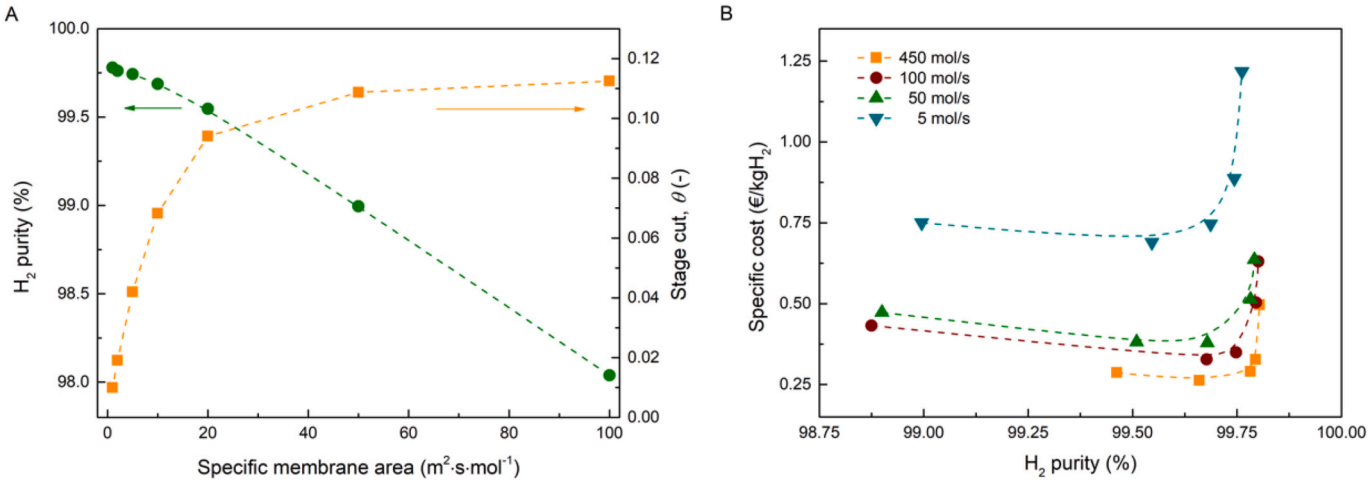

Fig. 12. (A) Hydrogen permeate concentration and stage cut as a function of the CMSM specific active separation area; (B) specific purified hydrogen cost from the natural gas network as a function of the H_2 purity for the four different feed flow rates.

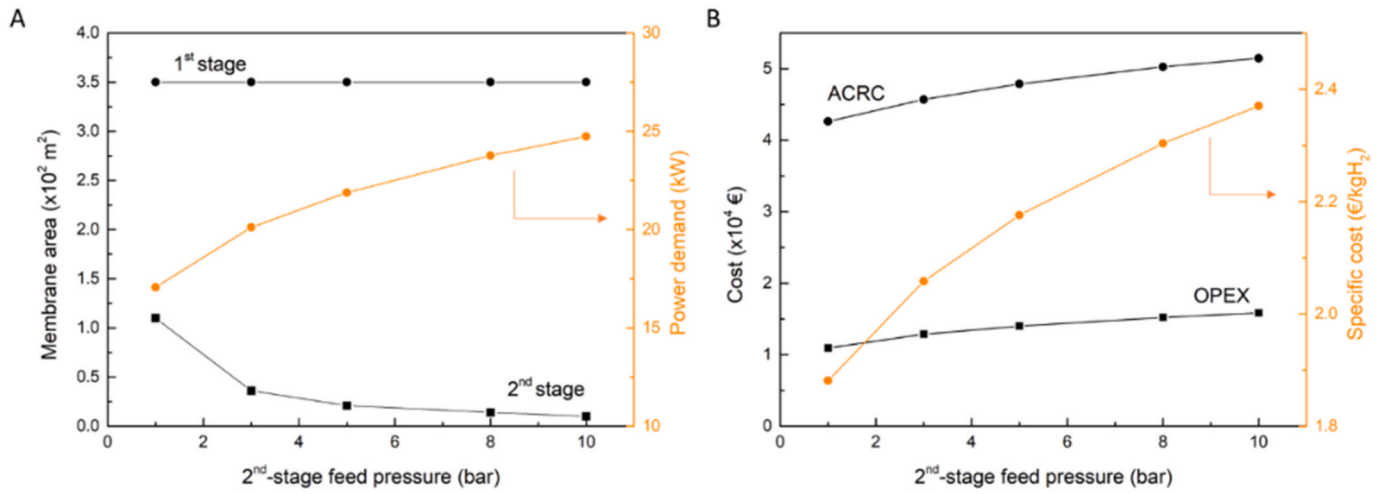

Fig. 13. Optimization of the 2nd stage feed pressure by the membrane area and power demand (A); and (B) Annual capital-related costs, OPEX and hydrogen purified specific cost as a function of the 2nd stage feed pressure.

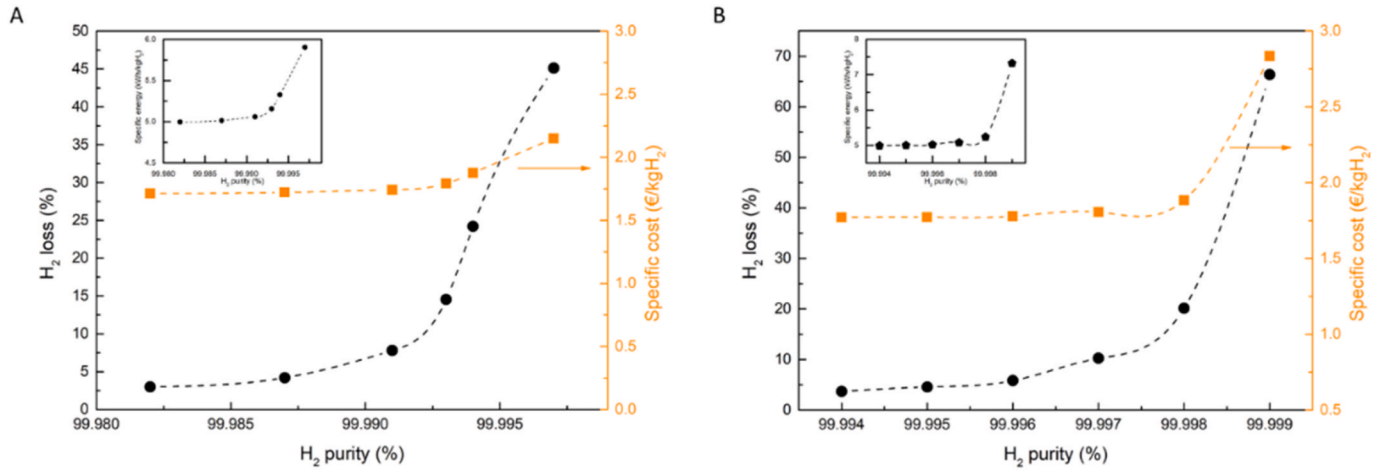

Fig. 14. H_2 loss, purified H_2 specific cost, and energy consumption as a function of the H_2 purity recovered from two stages CM0H22 (A) and CM0H22 + CM1H11 (B). The lines were added to guide the eyes.

purity at competitive costs. A two-stage system using CM1H11 membranes allowed the recovery of *ca.* 96.2 % of the hydrogen to a concentration >99.997 % for 1.88 €·kgH_2^{-1}. This result is extremely competitive: to obtain H_2 at the same concentration and recovery conditions, the PSA separation technology presents a separation cost of 7.3 €·kgH_2^{-1} [17]. The high separation cost for PSA technology is related to the fact that the component present in higher concentration – methane – is the adsorbed one: so, larger adsorbent columns are required (high CAPEX value). Besides, to return to the grid the purged natural gas, it is necessary to re-pressurize it, making the PSA approach even more expensive. On the other hand, palladium and carbon membranes supported on ceramics have a separation cost of *ca.* 5 €·kgH_2^{-1} [16].

3.7. Conclusions

Green, low-cost, highly reproducible, and easy-to-scale-up cellulose-based CMSM were successfully fabricated. A polymer precursor solution was optimized to originate a highly selective CMSM (CM1H11), with a permeability to H_2 of 500 barrer and an H_2/CH_4 permselectivity of *ca.* 3500, which corresponds to a Robeson index of 100. Furthermore, an increase in the CMSM permeability to H_2 was obtained after a consistent optimization of the carbonization conditions. Hydrogen was introduced in the carbonization purging atmosphere, and an increase in the pore size was observed, producing a more permeable CMSM but reducing the membrane selectivity. After optimizing the carbonization conditions, a CMSM (CM0H22) was prepared with permeability to H_2 of 1300 barrer and with the following permselectivities: H_2/CH_4 of 1082, H_2/CO_2 of 3.9, and H_2/N_2 of 14.

The membranes fabricated in this work display high separation performance for hydrogen recovery from natural gas networks (H_2/CH_4), CO_2 from reforming or gasification (H_2/CO_2), and hydrogen recovery from industrial processes (ammonia production, refineries, or syngas). The separation performance of 50 days aged CM0H22 membrane was assessed at different temperatures, feed pressures, and humidity. It was concluded that the humidity did not impair the separation performance of the prepared membrane.

A techno-economic analysis of recovering hydrogen from the natural gas grids with different target concentrations using CMSM membranes was also performed. It was concluded that a single stage of carbon membranes allows the production of a permeate stream with a maximum H_2 concentration of 99.8 %. An extremely competitive hydrogen purification cost of 0.26 €·kgH_2^{-1} was obtained for medium-scale industrial applications of these CMSMs (feed flow rate of 450 mol·s^{-1}) using membrane CM1H11 with an area of 5000 m^2 and a recovery of 68 %. The use of a second membrane stage, also employing membrane CM1H11, was studied to produce a high-purity permeate

stream. For 1 bar of feed pressure to the second stage, it was computed a permeate flow rate of 83 kg of H_2 per day (suitable to fuel two Toyota Mirai), a membrane area of 460 m^2 and an energy consumption of 4.87 $kWh \cdot kgH_2^{-1}$, which corresponds to an extremely high hydrogen recovery from of 96 % and a highly competitive cost of 1.88 $€ \cdot kgH_2^{-1}$.

The results presented in this work demonstrate that CMSMs produced from a cellulose precursor are in the pole position for recovering and purifying hydrogen from several sources critical for the world's energy decarbonization effort.

CRediT authorship contribution statement

Tiago Araújo: Conceptualization, Data curation, Formal analysis, Investigation, Methodology, Project administration, Validation, Writing – original draft. **Gabriel Bernardo:** Writing – review & editing. **Adélio Mendes:** Conceptualization, Funding acquisition, Project administration, Resources, Supervision, Writing – review & editing.

Declaration of competing interest

The authors declare that they have no known competing financial interests or personal relationships that could have appeared to influence the work reported in this paper.

Data availability

Data will be made available on request.

Acknowledgements

T. Araújo is grateful to the Portuguese Foundation for Science and Technology (FCT) for the doctoral grant (reference SFRH/BD/143598/2019) supported by POPH/FSE. G. Bernardo thanks the Portuguese Foundation for Science and Technology (FCT) for the financial support of his work contract through the Scientific Employment Stimulus Individual Call – (CEEC_IND/02039/2018). The authors acknowledge the European Commission through the European Union's Horizon 2020 program - FET Proactive research and innovation action - under grant agreement No. 952219 (112CO2). This work also was financially supported by LA/P/0045/2020 (ALiCE), UIDB/00511/2020 and UIDP/00511/2020 (LEPABE), funded by national funds through FCT/MCTES (PIDDAC). The authors are thankful to Luciana Rocha from U. Aveiro for the SEM and XRD experiments, to CEMUP for XPS, to Luis Carlos Matos from U. Porto for Raman and INL for the TEM.

Appendix A. Supplementary data

Supplementary data to this article can be found online at https://doi.org/10.1016/j.memsci.2023.122337.

References

[1] N. Mac Dowell, P.S. Fennell, N. Shah, G.C. Maitland, The role of CO2 capture and utilization in mitigating climate change, Nat. Clim. Change 7 (2017) 243–249.
[2] Z. Abdin, A. Zafaranloo, A. Rafiee, W. Mérida, W. Lipiński, K.R. Khalilpour, Hydrogen as an energy vector, Renew. Sustain. Energy Rev. 120 (2020), 109620.
[3] IEA, Global, Hydrogen Demand by Sector in the Sustainable Development Scenario, 2019 -2070, p. 2020.
[4] L. Huang, Z. Xing, X. Zhuang, J. Wei, Y. Ma, B. Wang, X. Jiang, X. He, L. Deng, Z. Dai, Polymeric membranes and their derivatives for H2/CH4 separation: state of the art, Separ. Purif. Technol. 297 (2022), 121504.
[5] A. Al-Qahtani, B. Parkinson, K. Hellgardt, N. Shah, G. Guillen-Gosalbez, Uncovering the true cost of hydrogen production routes using life cycle monetisation, Appl. Energy 281 (2021), 115958.
[6] H. Nazir, C. Louis, S. Jose, J. Prakash, N. Muthuswamy, M.E.M. Buan, C. Flox, S. Chavan, X. Shi, P. Kauranen, T. Kallio, G. Maia, K. Tammeveski, N. Lymperopoulos, E. Carcadea, E. Veziroglu, A. Iranzo, A.M. Kannan, Is the H2 economy realizable in the foreseeable future? Part I: H2 production methods, Int. J. Hydrogen Energy 45 (2020) 13777–13788.
[7] C. Wulf, M. Reuß, T. Grube, P. Zapp, M. Robinius, J.-F. Hake, D. Stolten, Life Cycle Assessment of hydrogen transport and distribution options, J. Clean. Prod. 199 (2018) 431–443.
[8] A. Sartbaeva, V.L. Kuznetsov, S.A. Wells, P.P. Edwards, Hydrogen nexus in a sustainable energy future, Energy Environ. Sci. 1 (2008) 79–85.
[9] M.E. Demir, I. Dincer, Cost assessment and evaluation of various hydrogen delivery scenarios, Int. J. Hydrogen Energy 43 (2018) 10420–10430.
[10] J. Cui, M. Aziz, Techno-economic analysis of hydrogen transportation infrastructure using ammonia and methanol, Int. J. Hydrogen Energy 48 (2023) 15737–15747.
[11] K.R. Narayan, Hydrogen-Powered Long-Distance Transportation for Portugal, Instituto Superior Técnico, Lisbon, 2021.
[12] DGEG, Estratégia Nacional para o Hidrogénio (EN-H2), https://www.dgeg.gov.pt/pt/areas-transversais/relacoes-internacionais/politica-energetica/estrategia-nacional-para-o-hidrogenio-en-h2/, 2020.
[13] S. Cerniauskas, A. Junco, T. Grube, M. Robinius, D. Stolten, Options of natural gas pipeline reassignment for hydrogen: cost assessment for a Germany case study, Int. J. Hydrogen Energy 45 (2020).
[14] M. Melaina, O. Sozinova, M. Penev, Blending Hydrogen into Natural Gas Pipeline Networks: A Review of Key Issues, 2013.
[15] L. Dehdari, I. Burgers, P. Xiao, K.G. Li, R. Singh, P.A. Webley, Purification of hydrogen from natural gas/hydrogen pipeline mixtures, Separ. Purif. Technol. 282 (2022), 120094.
[16] M. Nordio, S.A. Wassie, M. Van Sint Annaland, D.A. Pacheco Tanaka, J.L. Viviente Sole, F. Gallucci, Techno-economic evaluation on a hybrid technology for low hydrogen concentration separation and purification from natural gas grid, Int. J. Hydrogen Energy 46 (2021) 23417–23435.
[17] M. Nordio, J. Melendez, M. van Sint Annaland, D.A. Pacheco Tanaka, M. Llosa Tanco, F. Gallucci, Comparison between carbon molecular sieve and Pd-Ag membranes in H2-CH4 separation at high pressure, Int. J. Hydrogen Energy 45 (2020) 28876–28892.
[18] G. Bernardo, T. Araújo, T. da Silva Lopes, J. Sousa, A. Mendes, Recent advances in membrane technologies for hydrogen purification, Int. J. Hydrogen Energy 45 (2020) 7313–7338.
[19] E. Fernandez, J.A. Medrano, J. Melendez, M. Parco, J.L. Viviente, M. van Sint Annaland, F. Gallucci, D.A. Pacheco Tanaka, Preparation and characterization of metallic supported thin Pd–Ag membranes for hydrogen separation, Chem. Eng. J. 305 (2016) 182–190.
[20] A.B. Fuertes, T.A. Centeno, Preparation of supported carbon molecular sieve membranes, Carbon 37 (1999) 679–684.
[21] M. Rungta, G.B. Wenz, C. Zhang, L. Xu, W. Qiu, J.S. Adams, W.J. Koros, Carbon molecular sieve structure development and membrane performance relationships, Carbon 115 (2017) 237–248.
[22] L. Lei, L. Bai, A. Lindbråthen, F. Pan, X. Zhang, X. He, Carbon membranes for CO2 removal: status and perspectives from materials to processes, Chem. Eng. J. 401 (2020), 126084.
[23] C. Zhang, W.J. Koros, Ultraselective carbon molecular sieve membranes with tailored synergistic sorption selective properties, Adv. Mater. 29 (2017), 1701631.
[24] N. Widiastuti, A.R. Widyanto, I.S. Caralin, T. Gunawan, R. Wijiyanti, W.N. Wan Salleh, A.F. Ismail, M. Nomura, K. Suzuki, Development of a P84/ZCC composite carbon membrane for gas separation of H2/CO2 and H2/CH4, ACS Omega 6 (2021) 15637–15650.
[25] D. Torres, S. Pérez-Rodríguez, L. Cesari, C. Castel, E. Favre, V. Fierro, A. Celzard, Review on the preparation of carbon membranes derived from phenolic resins for gas separation: from petrochemical precursors to bioresources, Carbon 183 (2021) 12–33.
[26] M.A. Llosa Tanco, J.A. Medrano, V. Cechetto, F. Gallucci, D.A. Pacheco Tanaka, Hydrogen permeation studies of composite supported alumina-carbon molecular sieves membranes: separation of diluted hydrogen from mixtures with methane, Int. J. Hydrogen Energy 46 (2021) 19758–19767.
[27] S.C. Rodrigues, R. Whitley, A. Mendes, Preparation and characterization of carbon molecular sieve membranes based on resorcinol–formaldehyde resin, J. Membr. Sci. 459 (2014) 207–216.
[28] S.C. Rodrigues, M. Andrade, J. Moffat, F.D. Magalhães, A. Mendes, Preparation of carbon molecular sieve membranes from an optimized ionic liquid-regenerated cellulose precursor, J. Membr. Sci. 572 (2019) 390–400.
[29] L. Lei, F. Pan, A. Lindbråthen, X. Zhang, M. Hillestad, Y. Nie, L. Bai, X. He, M. D. Guiver, Carbon hollow fiber membranes for a molecular sieve with precise-cutoff ultramicropores for superior hydrogen separation, Nat. Commun. 12 (2021) 268.
[30] P.H.T. Ngamou, M.E. Ivanova, O. Guillon, W.A. Meulenberg, High-performance carbon molecular sieve membranes for hydrogen purification and pervaporation dehydration of organic solvents, J. Mater. Chem. A 7 (2019) 7082–7091.
[31] T. Araújo, M. Andrade, G. Bernardo, A. Mendes, Stable cellulose-based carbon molecular sieve membranes with very high selectivities, J. Membr. Sci. 641 (2022), 119852.
[32] T. Araújo, A.J. Parnell, G. Bernardo, A. Mendes, Cellulose-based carbon membranes for gas separations - unraveling structural parameters and surface chemistry for superior separation performance, Carbon 204 (2023) 398–410.
[33] H. Guo, J. Wei, Y. Ma, Z. Qin, X. Ma, R. Selyanchyn, B. Wang, X. He, B. Tang, L. Yang, L. Yao, W. Jiang, Y. Zhuang, D. Yin, X. Li, Z. Dai, Carbon molecular sieve membranes fabricated at low carbonization temperatures with novel polymeric acid porogen for light gas separation, Separ. Purif. Technol. 317 (2023), 123883.
[34] L. Lei, A. Lindbråthen, X. Zhang, E.P. Favvas, M. Sandru, M. Hillestad, X. He, Preparation of carbon molecular sieve membranes with remarkable CO2/CH4

selectivity for high-pressure natural gas sweetening, J. Membr. Sci. 614 (2020), 118529.
[35] M. Campo, F. Magalhães, A. Mendes, Carbon molecular sieve membranes from cellophane paper, J. Membr. Sci. 350 (2010) 180–188.
[36] S.C. Rodrigues, M. Andrade, J. Moffat, F.D. Magalhães, A. Mendes, Carbon membranes with extremely high separation factors and stability, Energy Technol. 7 (2019), 1801089.
[37] Y. Ma, M.L. Jue, F. Zhang, R. Mathias, H.Y. Jang, R.P. Lively, Creation of well-defined "mid-sized" micropores in carbon molecular sieve membranes, Angew. Chem. Int. Ed. 58 (2019) 13259–13265.
[38] T. Araújo, G. Bernardo, A. Mendes, Cellulose-Based Carbon Molecular Sieve Membranes for Gas Separation: A Review, Molecules, 2020.
[39] T. Araújo, F. Barbosa, J.M. Sousa, G. Bernardo, A. Mendes, Preparation and characterization of free-standing composite cellulose-based carbon molecular sieve membranes, Int. J. Memb. Sci. Tech. 9 (2023) 116–127.
[40] M. Andrade, A.J. Parnell, G. Bernardo, A. Mendes, Propane selective carbon adsorbents from phenolic resin precursor, Microporous Mesoporous Mater. 320 (2021), 111071.
[41] F. Stoeckli, A. Slasli, D. Hugi-Cleary, A. Guillot, The characterization of microporosity in carbons with molecular sieve effects, Microporous Mesoporous Mater. - MICROPOROUS MESOPOROUS MAT 51 (2002) 197–202.
[42] F. Stoeckli, T.A. Centeno, On the characterization of microporous carbons by immersion calorimetry alone, Carbon 35 (1997) 1097–1100.
[43] C. Nguyen, D.D. Do, Adsorption of supercritical gases in porous media: determination of micropore size distribution, J. Phys. Chem. B 103 (1999) 6900–6908.
[44] C. Nguyen, D.D. Do, K. Haraya, K. Wang, The structural characterization of carbon molecular sieve membrane (CMSM) via gas adsorption, J. Membr. Sci. 220 (2003) 177–182.
[45] S.C. Rodrigues, M. Andrade, J. Moffat, F.D. Magalhaes, A. Mendes, Carbon membranes with extremely high separation factors and stability, Energy Technol. 7 (2019).
[46] D. Chen, F. Yang, D.S. Karousos, L. Lei, E.P. Favvas, X. He, Process parametric testing and simulation of carbon membranes for H2 recovery from natural gas pipeline networks, Separ. Purif. Technol. 307 (2023), 122842.
[47] X. He, L. Lei, Z. Dai, Green hydrogen enrichment with carbon membrane processes: techno-economic feasibility and sensitivity analysis, Separ. Purif. Technol. 276 (2021), 119346.
[48] X. He, D. Chen, Z. Liang, F. Yang, Insight and comparison of energy-efficient membrane processes for CO2 capture from flue gases in power plant and energy-intensive industry, Carbon Capt. Sci. Tech. 2 (2022), 100020.
[49] X. He, Y. Chu, A. Lindbråthen, M. Hillestad, M.-B. Hägg, Carbon molecular sieve membranes for biogas upgrading: techno-economic feasibility analysis, J. Clean. Prod. 194 (2018) 584–593.
[50] S. Haider, A. Lindbråthen, J.A. Lie, M.-B. Hägg, Carbon membranes for oxygen enriched air – Part II: techno-economic analysis, Separ. Purif. Technol. 205 (2018) 251–262.
[51] J. Gong, J. Li, J. Xu, Z. Xiang, L. Mo, Research on cellulose nanocrystals produced from cellulose sources with various polymorphs, RSC Adv. 7 (2017) 33486–33493.
[52] A.D. French, Idealized powder diffraction patterns for cellulose polymorphs, Cellulose 21 (2014) 885–896.
[53] M.a. Fauziyah, W. Widiyastuti, R. Balgis, H. Setyawan, Production of cellulose aerogels from coir fibers via an alkali–urea method for sorption applications, Cellulose 26 (2019) 9583–9598.
[54] C. Azenha, C. Mateos-Pedrero, T. Lagarteira, A.M. Mendes, Tuning the selectivity of Cu2O/ZnO catalyst for CO2 electrochemical reduction, J. CO2 Util. 68 (2023), 102368.
[55] Y. Ma, M. Jue, F. Zhang, R. Mathias, H. Jang, R. Lively, Creation of well-defined "mid-sized" micropores in carbon molecular sieve membranes, Angew. Chem. 131 (2019).
[56] Y.-R. Rhim, D. Zhang, D.H. Fairbrother, K.A. Wepasnick, K.J. Livi, R.J. Bodnar, D. C. Nagle, Changes in electrical and microstructural properties of microcrystalline cellulose as function of carbonization temperature, Carbon 48 (2010) 1012–1024.
[57] A.C. Ferrari, J. Robertson, Interpretation of Raman spectra of disordered and amorphous carbon, Phys. Rev. B 61 (2000) 14095–14107.
[58] A. Sadezky, H. Muckenhuber, H. Grothe, R. Niessner, U. Pöschl, Raman microspectroscopy of soot and related carbonaceous materials: spectral analysis and structural information, Carbon 43 (2005) 1731–1742.
[59] L.M. Robeson, The upper bound revisited, J. Membr. Sci. 320 (2008) 390–400.
[60] R. Swaidan, B. Ghanem, I. Pinnau, Fine-tuned intrinsically ultramicroporous polymers redefine the permeability/selectivity upper bounds of membrane-based air and hydrogen separations, ACS Macro Lett. 4 (2015) 947–951.
[61] W. Ogieglo, T. Puspasari, X. Ma, I. Pinnau, Sub-100 nm carbon molecular sieve membranes from a polymer of intrinsic microporosity precursor: physical aging and near-equilibrium gas separation properties, J. Membr. Sci. 597 (2020), 117752.
[62] J. Liang, Z. Wang, M. Huang, S. Wu, Y. Shi, Y. Zhang, J. Jin, Effects on carbon molecular sieve membrane properties for a precursor polyimide with simultaneous flatness and contortion in the repeat unit, ChemSusChem 13 (2020) 5531–5538.
[63] L. Ding, Y. Wei, L. Li, T. Zhang, H. Wang, J. Xue, L.-X. Ding, S. Wang, J. Caro, Y. Gogotsi, MXene molecular sieving membranes for highly efficient gas separation, Nat. Commun. 9 (2018) 155.